Wavefront engineering for mid-infrared and terahertz quantum cascade lasers [Invited]

Nanfang Yu[1,2] and Federico Capasso[1,3]

[1]*School of Engineering and Applied Sciences, Harvard University, Cambridge, Massachusetts 02138, USA*
[2]*e-mail: nyu@fas.harvard.edu*
[3]*e-mail: capasso@seas.harvard.edu*

Received July 2, 2010; revised August 12, 2010; accepted August 19, 2010;
posted August 24, 2010 (Doc. ID 131032); published October 11, 2010

We review our recent work on beam shaping of mid-infrared (mid-IR) and terahertz (THz) quantum cascade lasers (QCLs) using plasmonics. Essentials of QCLs are discussed; these include key developments, the operating principle based on quantum design, and beam quality problems associated with laser waveguide design. The bulk of the present paper is focused on the use of surface plasmons (SPs) to engineer the wavefront of QCLs. This is achieved by tailoring the SP dispersion using properly designed plasmonic structures, in particular, plasmonic Bragg gratings, designer (spoof) surface plasmon structures, and channel polariton structures. Using mid-IR and THz QCLs as a model system, various functionalities have been demonstrated, ranging from beam collimation, polarization control, to multibeam emission and spatial wavelength demultiplexing. Plasmonics offers a monolithic, compact, and low-loss solution to the problem of poor beam quality of QCLs and may have a large impact on applications such as sensing, light detection and ranging (LIDAR), free-space optical communication, and heterodyne detection of chemicals. The plasmonic designs are scalable and applicable to near-infrared active or passive optical devices.

OCIS codes: 140.5965, 140.3070, 250.5403, 240.6680, 240.6690, 160.3918, 140.3300, 120.1680.

1. QUANTUM CASCADE LASER DESIGN AND OPERATION

A. Introduction

That light amplification is possible in intersubband transitions, i.e., transitions between quantized energy states within one energy band of a semiconductor, was first predicted by Kazarinov and Suris in 1971 in a seminal paper [1]. The first quantum cascade laser (QCL), based on such principle, was invented and demonstrated [2] at Bell Labs in 1994 by Faist, Capasso, Sivco, Hutchinson, and Cho. The first prototypes operated only in pulsed mode at a maximum temperature of ~90 K. Advancements in band-engineering and waveguide designs led within a few years to many important achievements: pulsed room temperature operation, continuous wave (CW) and single-mode operation, extension of the operating wavelength to values as short as 3.5 μm and as long as 19 μm, ultrashort pulse operation, and the first applications to spectroscopy and chemical sensing [3,4]. At first, QCLs had to be cooled to about 100 K to operate CW and operated multimode on several Fabry–Perot modes of the laser cavity formed by the cleaved ends of the laser waveguide. In 2002, CW room-temperature operation was achieved [5], and since then continuous improvements in the design, material quality, fabrication, and thermal management have led to record optical power of ~120 W pulsed [6] and ~3.0 W CW [7,8] at room temperature. The corresponding CW power efficiency for these Fabry–Perot cavity devices was 16.5% at 4.8 μm [7] and 13% at 4.6 μm [8]. The development of single-mode QCLs, essential for the narrow linewidth operation required for high-resolution spectroscopy, started soon after the first QCL report by embedding in the laser cavity a grating that introduced distributed feedback (DFB) [9,10].

In the last few years, QCLs operating at near room temperature with broad gain profiles have become available and have been incorporated into external cavities to produce tuning ranges with a single QCL of ~200 cm^{-1} CW and ~400 cm^{-1} pulsed [11–17]. In a recent development, an array of 32 DFB lasers on a single chip covering about 100 cm^{-1} in pulsed mode has been reported [18] making possible the creation of broadly tunable subminiature mid-infrared (mid-IR) laser sources for spectroscopy. The tuning range of this source was recently increased to 220 cm^{-1} using a 24-laser array [19].

AlInAs/GaInAs grown on InP substrate is the material of choice for mid-IR QCLs. The original lasers were produced using only molecular beam epitaxy (MBE), owing to its ability to form atomically abrupt interfaces between layers of nanometer or even sub-nanometer thickness. However, a properly designed metalorganic chemical vapor deposition (MOCVD) reactor can approach the interface abruptness associated with MBE. Detailed studies of MOCVD grown QCLs operating at 4.6, 5.2, and 8.3 μm wavelength have shown that their pulsed and CW performance at room temperature is comparable to that of MBE grown QCLs [20,21].

The first THz QCL lasing at 4.4 terahertz (THz) (λ_o ~67 μm) was demonstrated by Köhler *et al.* at the Scuola Normale Superiore in Pisa, Italy, in collaboration with Cambridge University [22]. These first devices operated in pulsed mode with peak power of a few mW and lased only up to several tens of Kelvin. Intensive research over the past few years has produced rapid improvements

[23–25]. At present, spectral coverage has been demonstrated from 0.84–5.0 THz [26,27]. Record operating temperature is 186 K, pulsed [28], and 117 K, CW [29]. The output power can routinely reach a few tens of mW, up to a couple of hundred mW for both pulsed and CW operations [30].

B. QCL Operating Principle

Laser diodes emitting at wavelengths ranging from the near-infrared to the visible are the workhorses of widespread technologies such as optical communications, optical recording (CD players, etc.), supermarket scanners, laser printers, fax machines, and laser pointers. The operating principle of these lasers is fundamentally simple: electrons and holes are electrically injected into an active region made of semiconductor materials where they recombine, giving off laser photons of wavelength close to the bandgap of the active region. A corollary of this is that if one wishes to build diode lasers emitting at very different wavelengths, one needs to choose materials with widely different bandgaps and electronic and optical properties. In spite of its simplicity and general nature, the diode laser principle has proven hard to extend to the mid- and far-infrared while maintaining the same level of performance of its shorter wavelength counterparts. The reason is that, as the bandgap shrinks in a semiconductor laser, its operation becomes much more critical in terms of the maximum operating temperature and temperature stabilization. In addition, as the bandgap shrinks, chemical bonds become weaker; this increased material "softness" facilitates the introduction of defects during growth and device fabrication, making diode lasers less reliable and reducing device yields. For example, semiconductor laser diodes made of lead salts [31,32] and emitting in the mid-IR, which have been used for many years in tunable laser spectroscopy, suffer from all of these limits.

The QCL overthrows the operating principle of conventional semiconductor lasers by relying on a radically different process for light emission, which is independent of the bandgap. Instead of using opposite charge carriers in semiconductors (electrons and holes) at the bottom of their respective conduction and valence bands, which recombine to produce light of frequency $v \approx E_g/h$, where E_g is the energy bandgap and h is Planck's constant, QCLs use only one type of charge carrier (electrons) that undergo quantum jumps between energy levels E_n and E_{n-1} to create a laser photon of frequency $(E_n - E_{n-1})/h$. These energy levels do not exist naturally in the constituent materials of the active region but are artificially created by structuring the active region in ultrathin layers known as quantum wells of nanometric thickness. The motion of electrons perpendicular to the layer interfaces is quantized and characterized by energy levels whose difference is determined by the thickness of the wells and by the height of the energy barriers separating them. The implications of this new approach, based on decoupling light emission from the bandgap by utilizing instead optical transitions between quantized electronic states, are many and far-reaching, amounting to a laser with entirely different operating characteristics from laser diodes and far superior performance and functionality.

C. Quantum Design

In QCLs, unlike in a laser diode, an electron remains in the conduction band after emitting a laser photon. The electron can therefore easily be recycled by being injected into an adjacent identical active region, where it emits another photon, and so forth. To achieve this cascading emission of photons, active regions are alternated with doped electron injectors and an appropriate bias voltage is applied. The active-region/injector stages of the QCL give rise to an energy staircase in which photons are emitted at each of the steps. The number of stages typically ranges from 20 to 50 for lasers designed to emit in the 4–8 μm range, and it is typically a couple of hundred for THz QCLs. This cascade effect is responsible for the high power that QCLs can attain.

The left panel of Fig. 1 illustrates a typical energy diagram of two stages of a mid-IR QCL designed to operate at wavelength $\lambda_o = 7.5$ μm, which serves to illustrate the key operating principle. The tilt in the conduction band is produced by the applied electric field. Note that each stage comprises an electron injector and an active region. The latter contains three quantized states; the laser transition is defined by the energy difference between states 3 and 2, which is determined primarily by the chosen thickness of the two wider wells. A population inversion between levels 3 and 2 is required for laser action. This translates to a requirement that the lifetime of level 3 should be substantially longer than the lifetime of state 2. To achieve that, the lowest level 1 is positioned about one optical phonon energy (~34 meV for InP) below level 2; this ensures that electrons in the latter state rapidly scatter by emission of an optical phonon to energy level 1. Because of its resonant nature, this process is very fast, characterized by a relaxation time of the order of 0.1–0.2 ps. Electrons in level 3 have instead a substantially longer lifetime, because of the much larger energy difference between states 3 and 2, so that the electron–phonon scattering process between the two states is nonresonant. To achieve lasing, however, one must also suppress the unwanted escape route by tunneling from state 3 to states on the right-hand side, which form a broad quasi-continuum. Such escape would reduce the level 3 population. To prevent this occurrence, one designs the

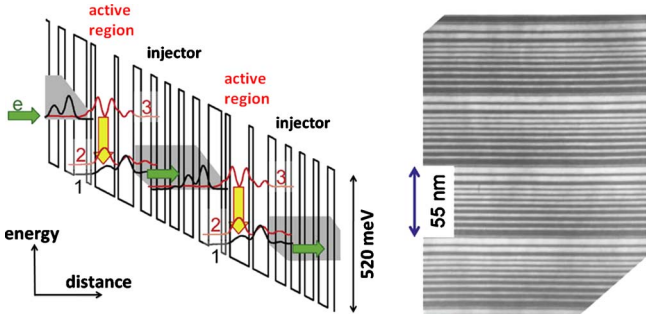

Fig. 1. (Color online) Left: Energy diagram of a quantum cascade laser emitting at $\lambda_o = 7.5$ μm. The energy levels and the corresponding probability distributions obtained from solving Schrödinger's equation are shown. The energy wells and barriers are made of GaInAs and AlInAs, respectively. Right: Transmission electron micrograph of a portion of the layer structure of an exemplary QCL. The dark and light layers correspond to the barriers and wells, respectively.

injector of the next stage as a superlattice such that, at energy corresponding to E_3, there is no resonant electronic state but rather a region of low density of states known as a mini-gap. Notice, instead, the dense manifold of states (a mini-band) facing levels 2 and 1, which favors efficient electron extraction from the active region. Finally, note that electrons are injected into the upper laser level by a process known as resonant tunneling, which ensures highly selective injection when the applied voltage is increased above a certain value.

The task of demonstrating THz QCLs is considerably more difficult than the mid-IR primarily because it takes special care to selectively inject electrons and depopulate them from closely spaced subbands ($\sim 4-20$ meV) in order to achieve the population inversion.

D. Waveguide Design and Beam Divergence Problem

Mid-IR QCLs are typically based on a dielectric waveguide structure in which the active core (i.e., active-region/injector layers) is embedded between semiconductors with smaller refractive indices; see Fig. 2(a). The active core is normally a couple of micrometers thick. As such, the output of edge-emitting mid-IR QCLs has the intrinsic problem of large beam divergence caused by diffraction at the small emission aperture. The divergence angle in the fast axis direction, i.e., perpendicular to the material layers, is typically a few tens of degrees. The divergence in the lateral direction along the slow axis depends on the waveguide width and is typically not smaller than a couple of tens of degrees. Increasing the waveguide width will decrease the lateral divergence. However, for a waveguide much larger than the effective wavelength in the waveguide, higher lateral modes are likely to coexist with or dominate over the fundamental mode, leading to multiple laser emissions in the lateral direction.

THz QCLs with the highest operating temperature and lowest threshold current to date take advantage of the high optical confinement (near 100%) and heat removal properties of a double-metal waveguide design, in which the laser active core, about 10 μm thick, is sandwiched between two metal strips [23–25]; see Fig. 2(b). However, this leads to non-Fresnel reflection at the subwavelength laser apertures, which gives rise to inefficient power outcoupling and poor beam quality. For example, the power reflectivity of laser modes at the aperture can be up to 90% [33], while it is ~30% according to Fresnel's formula (valid for plane waves and infinitely large interfaces). The laser emission is extremely divergent (divergence angle ~180° perpendicular to the semiconductor layers), and this represents a particularly serious problem for applications such as the far-infrared heterodyne detection of chemicals, since the output of THz QCLs (local oscillator) must be focused into a small-area Schottky diode mixer [34].

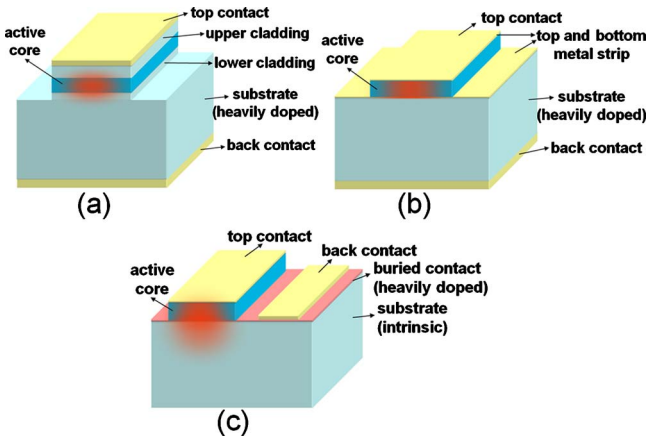

Fig. 2. (Color online) Waveguide designs. (a) Dielectric waveguide for mid-IR QCLs. (b) Double-metal waveguide for THz QCLs. (c) Single plasmon waveguide for THz QCLs. The confinement of the laser mode is based on surface waves bound to the top metallization and on the quasi-metallic confinement provided by a thin, heavily doped semiconductor buried contact layer placed below the active core. Schematics of laser waveguide modes are shown in red.

It is not practical to suppress the divergence in the fast axis direction by simply growing thick laser active cores. Such devices would require unrealistically high voltages for operation and would have heat dissipation problems.

Collimation of QCLs is conventionally conducted using lenses or parabolic mirrors. These optical components are usually bulky and need careful alignment; they are expensive because of a limited choice of infrared transparent materials (germanium, zinc selenide, polyethylene, etc.), thicker optical coatings compared to visible/near-infrared optics, and relatively fewer suppliers. In a similar approach, micro lenses [35] and metallic horn antennas [36] have been mounted onto laser apertures to reduce beam divergence and to enhance power output. However, this method requires meticulous manipulation and alignment of small optical components, which affects device yield and robustness.

QCLs that intrinsically produce small divergence beams are highly desirable; by using lenses of moderate numerical aperture for collimation such devices will be suitable for many applications. A number of approaches following this scheme have been demonstrated. First, mid-IR QCLs with tapered waveguides or wide-ridge waveguides have been demonstrated to emit diffraction-limited laser beams with significantly reduced lateral divergence [6,37–39]. Second, QCLs have been integrated with grating outcouplers. This approach relies on constructive interference between multiple surface emissions to reduce beam divergence. For example, mid-IR [40–43] and THz QCLs [44–46] with 1D integrated grating-outcouplers have shown greatly reduced beam divergence in the direction along laser ridges. Surface-emitting ring or disc QCLs with 2D second-order gratings have demonstrated collimation in two dimensions [47,48], but this does not solve the problem of vertical divergence. Third, QCLs have been processed into edge-emitting or surface emitting photonic crystal (PC) structures [49–52]. Such devices operate on photonic bandgap modes (microcavity) or photonic band-edge modes (DFB) and have been demonstrated to achieve controllable far-field emission patterns. The drawback of the surface emission scheme is that it results in device structures with reduced mode confinement and, therefore, increased laser threshold current density, which will probably lead to reduced maximum device operating temperatures in CW operation.

2. PLASMONICS FOR INFRARED LIGHT

A. The Elusive Mid- and Far-Infrared Surface Plasmons

Because of the strong limitations of dielectric-based optical components in the mid- and far-infrared, plasmonic structures are increasingly regarded as the media of choice in this wavelength range. Plasmonics involves manipulation of surface plasmons (SPs), which are collective oscillations of surface electrons in metals interacting with electromagnetic fields [53–55]. This can happen when electromagnetic radiation is scattered by small metallic particles, and the first comprehensive theoretical treatment of the problem was provided by Mie in 1908 [56]. SPs also exist on a planar interface between a metal and a dielectric as electron density waves coupled to electromagnetic fields. In 1907, Zenneck studied a similar problem: the propagation of radio waves on the surface of the Earth [57]. SPs have been known for a long time, but it was not until two decades ago that researchers started to explore their extremely broad range of applications and new possibilities at the basic research level.

In contrast to conventional optical components, where light is controlled in three dimensions, plasmonic structures provide compact optical processing, where planar metallic structures are used to manipulate the amplitude and phase of SPs in two dimensions. Furthermore, plasmonic structures manipulate light with subwavelength precision. This is due to the large spatial frequency components associated with metallic structures with sharp features. Because of these advantages, one can envision integrating plasmonic structures on active optical devices to engineer their optical near-fields and far-fields at will.

Before going on to present results on high-performance QCLs integrated with plasmonic structures, there is a fundamental question we have to answer: are there "real" SPs at mid-IR wavelength and beyond? By "real" we mean having the key property of strong (i.e., subwavelength) confinement typical of SPs at visible frequencies.

It is known that the in-plane wavevector of SPs on a planar interface is [53–55]

$$\beta(\omega) = k_o \sqrt{\frac{\epsilon_d \epsilon_m(\omega)}{\epsilon_d + \epsilon_m(\omega)}}, \tag{1}$$

where ϵ_d and ϵ_m are, respectively, the permittivity of the dielectric and metal defining the interface, and k_o is the vacuum wavevector. While ϵ_d is, in general, weakly dependant of ω away from the restrahlen bands, ϵ_m is strongly dependent on ω, due to interactions between light and conduction electrons and interband electronic transitions in the metal. Because the two materials have very different dispersion properties, the in-plane wavevector β departs from k_o as frequency ω increases from zero, and the deviation reaches maximum when the real part of ϵ_m is negative and has an absolute value equal to ϵ_d (so the denominator of Eq. (1) is minimized). The frequency at which this condition is satisfied is called the asymptotic SP frequency, and it is usually in the visible or near-ultraviolet for metals. At mid-IR and THz frequencies, however, ϵ_m is two to three orders of magnitude larger than ϵ_d so that one can hardly distinguish the light line in the dielectric and the SP dispersion curve: $\beta(\omega) \approx k_o\sqrt{\epsilon_d}$. As a result, the out-of-plane wavevector (i.e., the decay rate of SPs in the dielectric normal to the interface) $|\kappa| = \sqrt{\beta^2 - k_o^2 \epsilon_d}$ is very small, corresponding to poorly confined surface waves, known as Sommerfeld or Zenneck waves [57,58]. In this regard, SPs in the real sense do not exist on planar metal/dielectric interfaces in the mid- and far-infrared wavelengths.

B. Three Approaches to Engineer Surface Plasmon Dispersion

Nanostructuring metal surfaces, however, changes the above picture completely. The simplest example is to texture a metal surface with a periodic structure, say, a grating with periodicity Λ. Like electron waves interacting with a periodic potential or light waves interacting with a photonic crystal, surface waves with certain frequencies experience strong Bragg diffractions from the grating so that they are forbidden to propagate on the surface [59]. In the dispersion diagram, small bandgaps open up in the vicinity of $\beta = m\pi/\Lambda$, m being an integer. Assuming we operate in a region close to one of these bandgaps where the dispersion curve deviates from the light line in the dielectric, the confinement of SPs, as a result, will be improved and we recover the essence of SPs. We will see in later sections that collimator designs based on $\beta \approx 2\pi/\Lambda$ (i.e., second-order grating) work well for mid-IR QCLs.

Next we ask the question: to what degree can one engineer the dispersion properties of SPs? The asymptotic SP frequency seems to be intrinsically determined by the properties of the interface materials: by introducing a simplified Drude model $\epsilon_m = 1 - \omega_p^2/\omega^2$ in the formula $\mathrm{Real}(\epsilon_m) = -\epsilon_d$, one obtains the asymptotic SP frequency

$$\omega_{sp} = \omega_p/\sqrt{1 + \epsilon_d}, \tag{2}$$

where $\omega_p = \sqrt{Ne^2/(\epsilon_0 m^*)}$ is the bulk plasma frequency, e, m^*, and N are the elementary charge, the effective mass, and the density of the conduction electrons, respectively. The expression for ω_p hints that the asymptotic SP frequency can be tuned by changing N. One such approach is to use doped semiconductors whose carrier concentrations are much lower than those in metals. This holds great promise for THz plasmonics: for example, it is estimated that GaAs with a doping level higher than above $n = 10^{17}$ cm^{-3} becomes metallic for 3 THz frequency light.

A completely different method to engineer the SP dispersion is to perforate metallic surfaces with subwavelength features. By introducing localized electromagnetic modes strongly interacting with the structured surfaces, one is able to reduce the asymptotic SP frequency by orders of magnitude into infrared and GHz frequency ranges. Such perforated surfaces are called designer plasmonic structures or "spoof" SP structures, as introduced by Pendry, Martín-Moreno, and García-Vidal [60,61] and observed on structured metals at THz frequencies [62].

Consider an array of grooves with subwavelength periodicity sculpted on the surface of a perfect metal (Fig. 3 left panel), the asymptotic frequency is given by [61]

$$\omega(\beta \to \infty) = \pi c/2h, \tag{3}$$

where h is the groove depth, and c is the speed of light in vacuum; see Fig. 3 right panel. Physically, Eq. (3) (or equivalently $h = \lambda_o/4$) corresponds to the first-order stand-

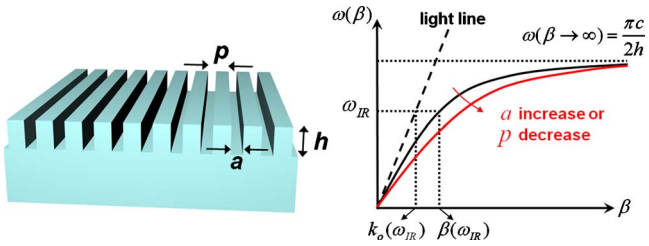

Fig. 3. (Color online) Left: By texturing a metal or a metallic semiconductor surface with subwavelength structures such as a 1D array of grooves, one can engineer the dispersion of SPs. Right: Schematic dispersion diagram for spoof SPs on a corrugated surface made from a perfect metal. The asymptote of the curve, $\omega(\beta\rightarrow\infty)$, the in-plane wavevector, β, and the out-of-plane wavevector, κ, can be tailored by changing the geometry of the grooves.

ing wave along the depth of the grooves: the phase accumulated during a roundtrip of the groove cavity mode is 2π (wavenumber times $2h$ contributes π, while the other π originates from reflection of the mode at the bottom of the grooves). As SPs strongly couple to the resonant cavity modes of the grooves, the group velocity of the SPs markedly reduces to near zero.

An alternative way to understand Eq. (3) is to treat each groove as a waveguide shorted at the end. According to transmission line theory, the input impedance of such terminated waveguide is [63]

$$\eta = i\,\eta_o \tan(k_o h), \tag{4}$$

where h, the groove depth, is now the length of the waveguide, and $\eta_o \sim 377\Omega$ is the free-space impedance. Equation (4) predicts that the impedance will be purely resistive if $h=\lambda_o/4$, while it will be inductive (capacitive) if $h<\lambda_o/4 (h>\lambda_o/4)$. Impedance being a real number means that current and voltage are in phase and therefore net power will flow into the grooves and eventually be dissipated through absorption. As a result, SPs can hardly propagate away from the launching spot, which is characteristic of spoof SPs near the asymptotic frequency.

Since $\omega(\beta\rightarrow\infty)$ is not directly associated with the interface materials, as in the case of conventional SPs, one can engineer the spoof SP dispersion curve and obtain a sizeable deviation between the curve and the light line at infrared frequencies, i.e., $\beta(\omega_{IR})>k_o(\omega_{IR})$ [60–62]; see Fig. 3(b) right panel. As a result, the out-of-plane wavevector $\kappa(\omega_{IR})=i\sqrt{\beta^2(\omega_{IR})-k_0^2(\omega_{IR})}$ can be large, corresponding to confined SPs with a 1/e decay distance in the air normal to the interface equal to $1/|\kappa|$ [62].

The two cases previously discussed both involve interaction between SPs and an assembly of surface textures. The difference is that the spoof SP structures explore the effective medium regime and therefore their effectiveness does not rely on collective behavior of a large number of elements as in the case of plasmonic Bragg gratings, where interference of waves coherently scattered by many periods is vital for their functionality. Because of this, spoof SP structures are more flexible in use: by stacking short sections of them with different geometries or by adiabatically tailoring the geometry of the constituent elements, complex optical devices can be built to manipulate SPs.

The third plasmonic structure involves interaction between SPs and a straight channel sculpted into a metallic surface. Such channel waveguides support the so-called channel polaritons that are featured by subwavelength confinement and moderate propagation losses [64–70]. Maradudin and others derived the exact dispersion relation of channel polaritons in channels with various cross-section shapes based on Green's theorem [64,65]; Bozhevolnyi and others used an effective index method for semi-quantitative modeling of channel polaritons [68–71], which is convenient and useful. Channel polariton modes are localized to the immediate vicinity of the channel and travel along it. The dispersion curves of these modes are well separated from that of SPs on a planar interface: channel polaritons have larger in-plane wavevectors, corresponding to increased effective mode indices n_{eff}.

In the simplest sense, channel waveguides are analogous to metal-insulator-metal (MIM) waveguides and the properties of channel polaritons can be understood from the perspective of transmission line theory. Let us treat the two walls of a channel groove as a pair of parallel perfect conducting strips. Assuming that the channel depth h is much larger than its width a, and that the propagating modes are transverse electromagnetic (TEM) waves, waveguide theory [63] predicts that the capacitance per unit length is $C=\epsilon_o h/a$, and the inductance per unit length is $L=\mu_o a/h$. As such, the characteristic impedance of the channel groove, modeled as a coplanar strip transmission line, will be

$$\eta_{wg} = \sqrt{L/C} = \eta_o a/h, \tag{5}$$

which is much smaller than η_o, the free-space impedance. Such a difference in impedance gives rise to localized channel polaritons. For constant width a, a deeper channel results in a larger impedance difference and therefore the modes are better confined with less fringing fields outside the channel grooves and less leakage into SPs on planar surfaces outside the channels. We will show in Section 7 that channel polaritons are employed to effectively spread THz energy over a large area on the laser facet, thereby reducing beam divergence in the far-field.

3. ONE-DIMENSIONAL COLLIMATORS FOR MID-IR QCLS

A. Design and Simulations

The 1D plasmonic collimator [72] consists of a slit aperture and a grating patterned on the metal-coated laser facet (Fig. 4 left panel). The structure is based on experimental and theoretical work on the beaming of optical radiation by aperture–groove structures [73,74]. The slit aperture and the grating grooves are oriented perpendicular to the laser polarization. The aperture is subwavelength in the vertical direction; it couples part of the laser emission into SPs propagating along the −z direction on the device facet (Fig. 4 left panel), where the plasmonic second-order grating (grating period $\Lambda\sim\lambda_{sp}$) coherently scatters their energy into the far-field, thereby breaking the diffraction limit set by the small emission area of the original laser.

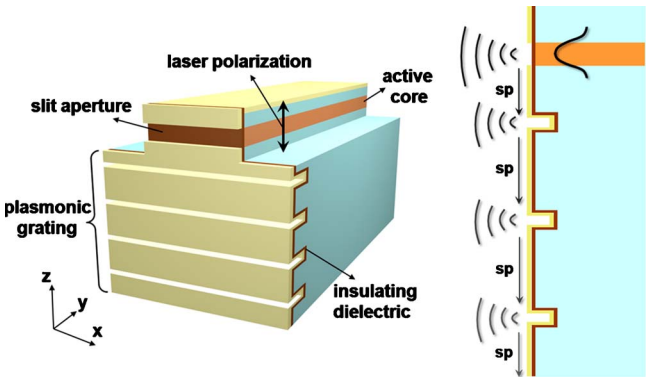

Fig. 4. (Color online) Left: Schematic of a 1D collimated laser. It comprises a QCL and a metallic aperture-grating structure defined on the facet. Right: Cross sections of the device. The grooves are sculpted directly into the laser facet using focused ion beam (FIB) milling, followed by conformal coatings of an insulating layer and an optically thick metal layer. FIB milling is used to finally open the slit aperture on the active core.

Plasmonic collimation is essentially an antenna array effect. We use as a figure of merit the concept of antenna directivity to characterize collimation in the vertical direction, and it is defined as $D=10\,log_{10}(2\pi I_{peak}/I_{total})$, where I_{peak} is the far-field peak intensity and I_{total} is the total intensity under the vertical beam profile.

We performed systematic 2D simulations to help design a structure with optimal beam directivity. It is critical to fine tune the groove width and depth so that the propagation distance of SPs on the facet is comparable to the length of the grating in the z direction. This ensures that the plasmonic grating scatters almost all the energy of the SPs into the far field and that maximum number of scattering elements are involved to minimize far-field divergence.

Figure 5(a) shows the simulated intensity distribution ($|E|^2$) of an unpatterned QCL; the laser beam is observed to diverge rapidly in the vertical direction outside the laser waveguide. As a comparison, Fig. 5(b) is a simulation for the device integrated with a plasmonic collimator consisting of 15 grating grooves with optimized geometry. It shows that many beams emerge from the entire patterned laser facet. Figure 5(c) is the calculated vertical far-field profile ($|E|^2$) for the collimated device: the full-width at half-maximum (FWHM) divergence angle of the central lobe is reduced from ~60° of the original device to 3.7°. The optical background is relatively uniform as a function of angle and has an average intensity less than 10% of the peak value. Figure 5(d) shows the electric-field distribution ($|E|$) around the slit and the first few grating grooves. The SPs are observed to localize within a distance of about one free-space wavelength from the device facet, indicating efficient coupling between the SP modes and the plasmonic structures; this is in sharp contrast to the weak interaction between mid-IR SPs and planar gold surfaces, where the decay distance of SPs in the air is estimated to be $\sim 10\lambda_o$. The latter case is demonstrated in Fig. 5(e), which shows that SPs are loosely bound to the metal/air interface for a device with a slit aperture and without the grating.

As discussed above, the reduction in far-field divergence is essentially an antenna array effect. Simulations

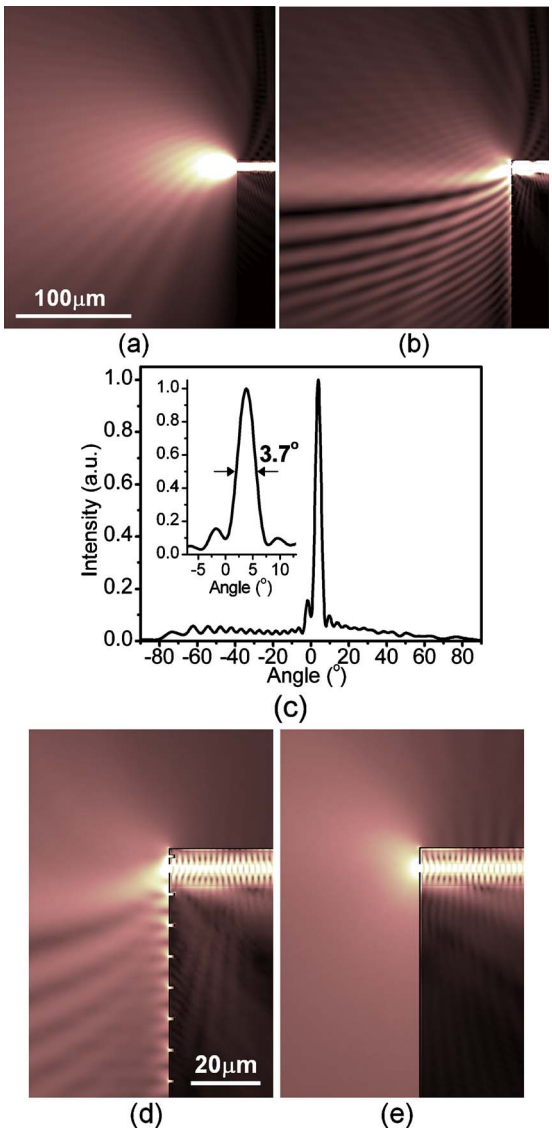

Fig. 5. (Color online) (a) Simulated intensity distribution ($|E|^2$) of an original unpatterned QCL emitting at $\lambda_o=9.9$ μm. The simulation plane is perpendicular to the laser materials layers and along the symmetry plane of the waveguide ridge. (b) Simulated intensity distribution of the QCL patterned with a plasmonic collimator. (c) Calculated far-field intensity distribution in the vertical direction for the device shown in (b); inset: zoom-in view of the central lobe. (d) Simulated electric-field distribution ($|E|$) around the slit and the first seven grating grooves. (e) Simulated electric-field distribution of a QCL with only the slit aperture.

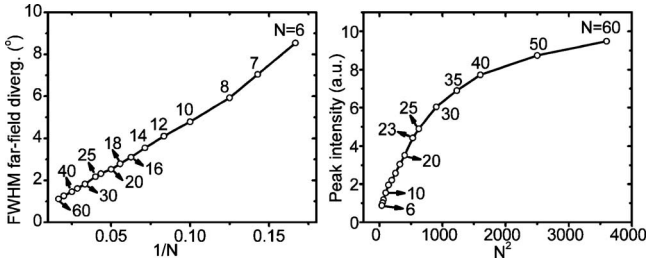

Fig. 6. Left: Simulation results showing the relation between far-field divergence angle and $1/N$, the inverse of the number of grating grooves. Right: Simulation results showing the relation between peak intensity of the far-field and N^2.

show that indeed the divergence angle is inversely proportional to the number of the grating grooves N at least up to $N=60$ (Fig. 6 left panel). The peak intensity in the far-field is proportional to N^2 up to $N=25$ (Fig. 6 right panel); for $N>25$, the effects of loss and lateral spreading of SPs give rise to a weaker variation of the peak intensity with N.

B. Experimental Results

Figures 7(a) and 7(b) show scanning electron microscope (SEM) images of a $\lambda_o=9.9$ μm QCL before and after patterning the 1D plasmonic collimator. The corresponding 2D far-field intensity distributions are presented in Figs. 7(c) and 7(d), respectively, demonstrating a strong reduction of the beam divergence in the vertical direction. The slight curvature of the far-field pattern in Fig. 7(d) is an edge effect due to the finite lateral size of the slit aperture. The line scans of the 2D far-field in the vertical direction are provided in Fig. 7(e), which shows that the divergence angle is reduced from about 62° to about 2.9° for the collimator with 20 grating grooves. The average intensity of the optical background is below 10% of the peak value. We note that there is no noticeable damage to the collimator after high peak-power operation (~100 mW peak power, pulsed mode). The beam quality factor M^2 of the device is determined to be about 2.5 based on measurements of the variation of the beam waist along the propagation direction. M^2 stands for the factor by which the divergence angle of a laser beam is larger than that of a Gaussian beam, assuming the two have the same beam waist. We calculated based on Figs. 7(c) and 7(d) that the directivity D is about 18 dB for the collimated device, while D is only about 7 dB for the original unpatterned laser. The lateral beam divergence after fabrication of the collimator is similar to that of the original laser. Figure 7(f) shows the light output versus current (LI) characteristics of the device, demonstrating a maximum output power of about 100 mW. We showed experimentally that the divergence angle is roughly inversely proportional to N and that devices with larger N have smaller average background and larger slope efficiencies; see Fig. 8.

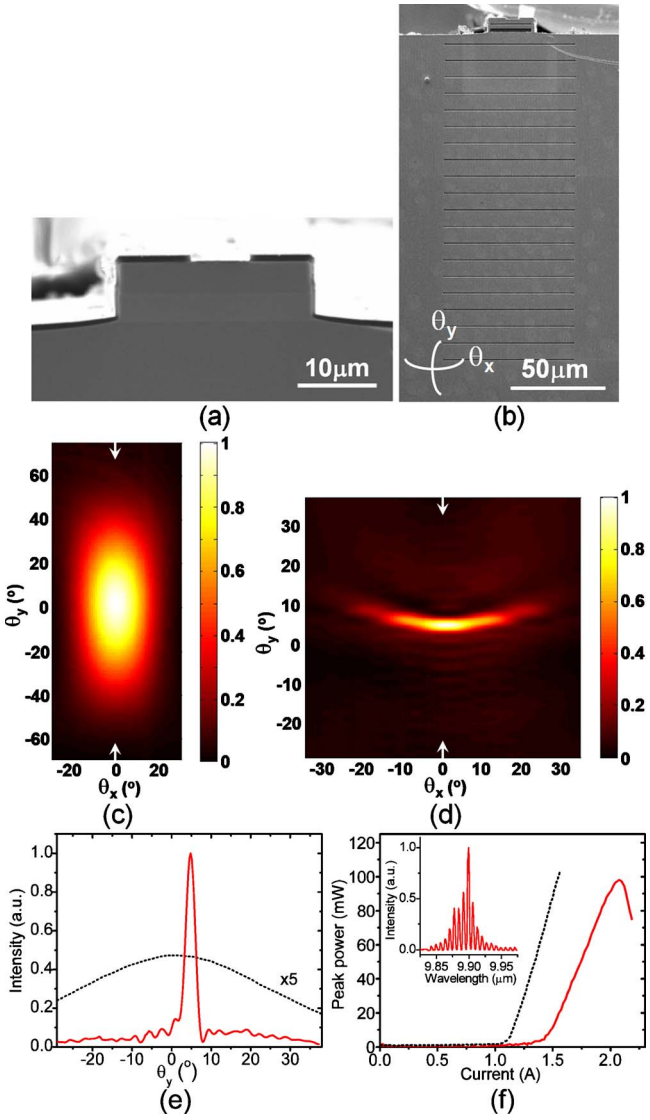

Fig. 7. (Color online) (a) and (b) SEM images of the facet of a $\lambda_o=9.9$ μm QCL before and after patterning a 1D plasmonic collimator. (c) and (d) Measured 2D far-field intensity distributions corresponding to (a) and (b), respectively. (e) Vertical line scans of (c) (black dotted curve) and (d) (red solid curve) along the arrows. (f) The black dotted curve and red solid curve are light output versus drive current (LI) characteristics of the unpatterned and patterned devices, respectively. Inset: spectrum of the collimated device taken at $I=1.8$ A.

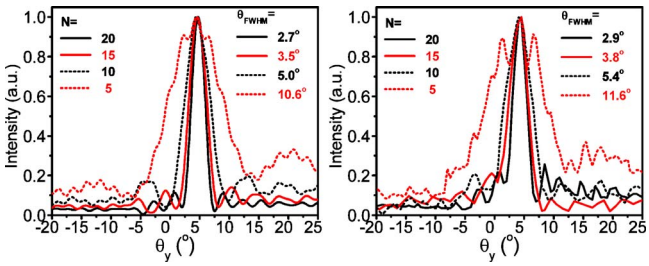

Fig. 8. (Color online) Left and right: Simulated and measured vertical far-field intensity profiles of devices with 1D collimators containing N grating grooves.

4. TWO-DIMENSIONAL COLLIMATORS FOR MID-IR QCLs

A. Design and Simulations

For 2D collimation [75,76], it is crucial to efficiently propagate SPs in two dimensions on the laser facet. We chose a design comprising a rectangular metal aperture and a circular plasmonic second-order grating; see Fig. 9.

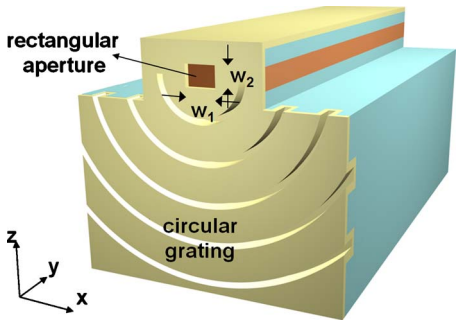

Fig. 9. (Color online) Schematic of a QCL integrated with a 2D plasmonic collimator.

SPs propagate preferentially in the vertical direction due to the TM polarization of QCLs. To efficiently launch SPs in the lateral direction, the width of the aperture w_1 has to be subwavelength, but this will limit power throughput. A trade-off is therefore to be sought between collimation and power output.

We performed systematic 3D simulations to study the evolution of the power outflow and the lateral spreading of SPs as a function of w_1 (Fig. 10). We increase w_1 in steps while maintaining the vertical aperture size w_2 to be approximately equal to the thickness of the laser active core ($\sim 2\ \mu$m). It is found that, for a small aperture ($2\ \mu\text{m} \times 2\ \mu\text{m}$), the SP spreading angle is very close to 90°, consistent with the divergence angle of radiation emitted by a dipolar emitter. When w_1 is nearly equal to $\lambda_o = 8.06\ \mu$m, the power throughput is improved by a factor of ~ 10 compared to $w_1 = 2\ \mu$m, while the lateral spreading of SPs is still significant.

B. Experimental Results

We fabricated 2D plasmonic collimators on $\lambda_o = 8.06\ \mu$m MOCVD-grown buried heterostructure (BHT) QCLs. A BHT device has regrowth regions on the lateral sides of the laser active core (Fig. 11(a)); it is more efficient in heat removal compared with ridge devices. The laser active core has a cross section of $2.1\ \mu\text{m} \times 9.7\ \mu$m and the initial divergence angles are $\theta_\parallel = 42°$ and $\theta_\perp = 74°$ in the lateral and vertical directions (Fig. 11(b)).

Figure 11(c) shows one representative device patterned with 20 circular grooves and a small aperture with $w_1 \times w_2 = 2.8\ \mu\text{m} \times 1.9\ \mu$m. The device exhibits greatly reduced divergence angles: $\theta_\parallel = 3.7°$ and $\theta_\perp = 2.7°$; see Fig. 11(d). The central lobe of the far-field contains about half of the total emitted power. The directivity D is about 8 dB for the unpatterned lasers, while it is about 27 dB after collimation. The beam quality factor M^2 of the device is about 2.0 in both the vertical and lateral directions.

We increased the lateral aperture size w_1 of the device stepwise using focused-ion beam (FIB) milling to investigate its impact on $\theta_\perp$, $\theta_\parallel$, and the power output. The vertical aperture size w_2 was kept constant at 1.9 μm. The LI characteristics for different aperture sizes are shown in Fig. 12(a). Larger w_1 corresponds to larger slope efficiency and therefore a higher maximum output power. As w_1 increases, the device experiences a gradual increase of the lasing threshold, due to decreased effective facet reflectivities.

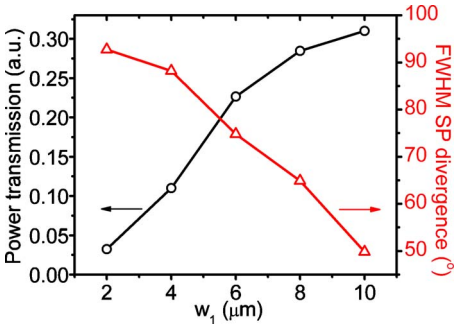

Fig. 10. (Color online) Simulated FWHM SP spreading angle and power throughput of the device with the 2D plasmonic collimator as a function of the lateral aperture size w_1.

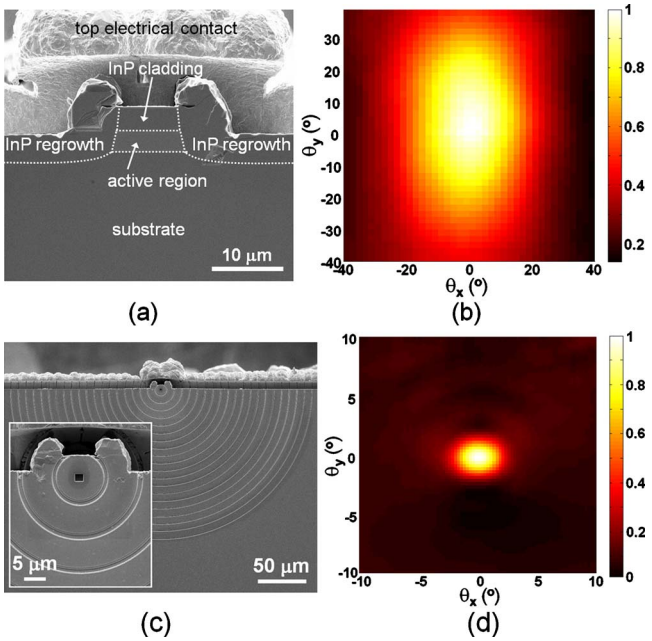

Fig. 11. (Color online) (a) SEM image showing the facet of an unpatterned $\lambda_o = 8.06\ \mu$m buried heterostructure QCL. (b) Measured emission pattern of the device in (a). (c) SEM image of the device with a 2D plasmonic collimator. Inset is zoom-in view. (d) Measured emission pattern of the device in (c).

Figure 12(b) summarizes the measured far-field beam divergence angles for different aperture sizes. As w_1 increases, the lateral divergence angle $\theta_\parallel$ increases due to less efficient lateral spreading of SPs, while $\theta_\perp$ remains essentially constant because the vertical propagation of SPs is insensitive to the change in aperture geometry. For the widest aperture $w_1 = 8.1\ \mu$m, the maximum output power is about 50% of that of the original unpatterned laser, while the divergence angles ($\theta_\perp = 2.4°$ and $\theta_\parallel = 4.6°$) are still significantly smaller than those of the original device.

5. MULTIBEAM QCLs

In plasmonic second-order gratings, the grating period is approximately equal to the SP wavelength, yielding a collimated beam normal to the laser facet. If instead the grating period differs from the SP wavelength, constructive interference will occur in a direction away from the facet normal.

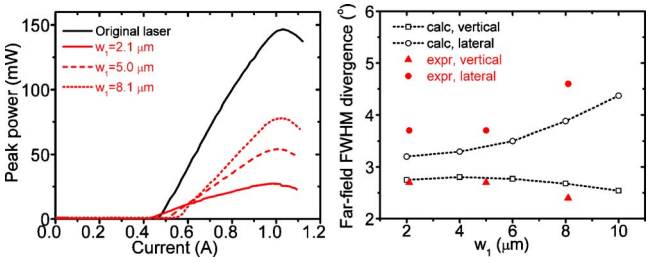

Fig. 12. (Color online) Left: LI characteristics for the device with a 2D plasmonic collimator. Right: Divergence angles in the vertical and lateral directions as a function of the lateral aperture size w_1.

We utilized this concept to split the emission of a single-wavelength QCL into two collimated beams in different directions [77]. Two successive plasmonic gratings with different periods and lengths can be defined on the device facet. By tuning the grating period, the emission direction of the beam originating from each individual grating can be controlled; by tuning the grating length (i.e., the number of grooves per grating), the intensity of the emitted beams can be independently controlled. Note that, since mid- and far-infrared SPs are able to propagate for significant distances comparable to at least hundreds of free–space wavelengths on a flat metal surface, several gratings can be patterned on the laser facet to produce multiple laser beams with controlled intensity and direction.

Figure 13 shows experimental and simulation results for a single-wavelength QCL emitting two beams. The grating closer to the aperture is designed to produce a beam propagating normal to the facet. The grating farther away from the aperture has a smaller grating period (Fig. 13 left panel). It provides a reciprocal lattice vector larger than the wavevector of the SPs, and therefore light diffracted from the grating is deflected away from the surface normal toward the top electrical contact of the device. The deflection angle is approximately 20° from the surface normal; see simulation and experimental results in Fig. 13 right panel.

Because the intensity of SPs decreases as they propagate through the grating grooves due to scattering from the grooves and Ohmic losses, the second grating was chosen to contain more grooves than the first one to allow the two emitted beams to have similar peak intensity; see Fig. 13 right panel.

To demonstrate lasers emitting spatially demultiplexed wavelengths, we used mid-IR QCLs with two stacks of active cores: one based on a two-phonon design emitting at ~10.5 μm and the other based on a bound-to-continuum (BTC) design emitting around ~9.3 μm [77]. It is essential to devise a plasmonic grating efficient in scattering light at both wavelengths. We chose a design that is the trade-off between the optimal structures for the two wavelengths.

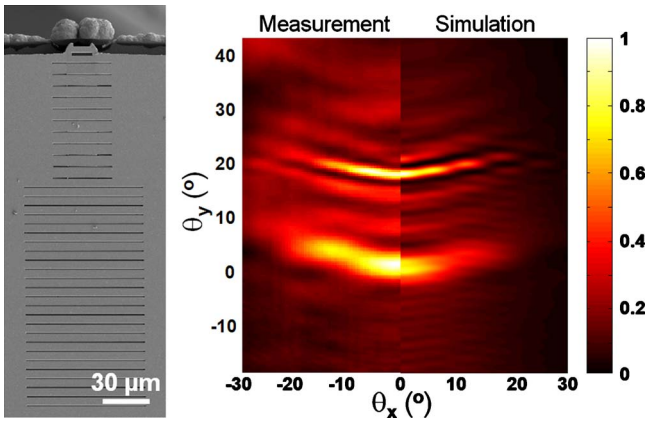

Fig. 13. (Color online) Left: SEM image of a $\lambda_o = 8.06$ μm QCL patterned with two plasmonic gratings. The grating closer to the aperture contains 11 grooves and has a 7.8-μm periodicity; the other grating contains 25 grooves and has a 6-μm periodicity. The latter has larger lateral dimensions to account for the lateral spreading of SPs. Right: Measured (left half) and simulated (right half) far-field emission patterns of the device.

Simulation and experimental results for a dual-wavelength device are presented in Fig. 14. A single grating with a periodicity of 8.5 μm was used; it deflects the $\lambda_o = 9.3$ μm component away from the facet normal toward the top contact by ~3° and the $\lambda_o = 10.5$ μm component by ~12°. The measured direction and divergence of the two beams are in good agreement with simulations; see Figs. 14(b) and 14(c).

The plasmonic beam splitter for single-wavelength lasers can be potentially useful for applications requiring a reference and a probe beam such as interferometry and holography. Our designs should be applicable to passive optical components. For example, the spatial wavelength demultiplexing component for dual-wavelength lasers can function as a demultiplexer for optical fibers.

6. MID-IR QCLs WITH INTEGRATED PLASMONIC POLARIZERS

Light sources with a desirable polarization state are essential for many applications. Polarization multiplexing is used in optical fiber communications and satellite communications to enhance data transmission rate; circularly polarized light is used in chemistry and biology for detecting molecules exhibiting circular dichroism. However,

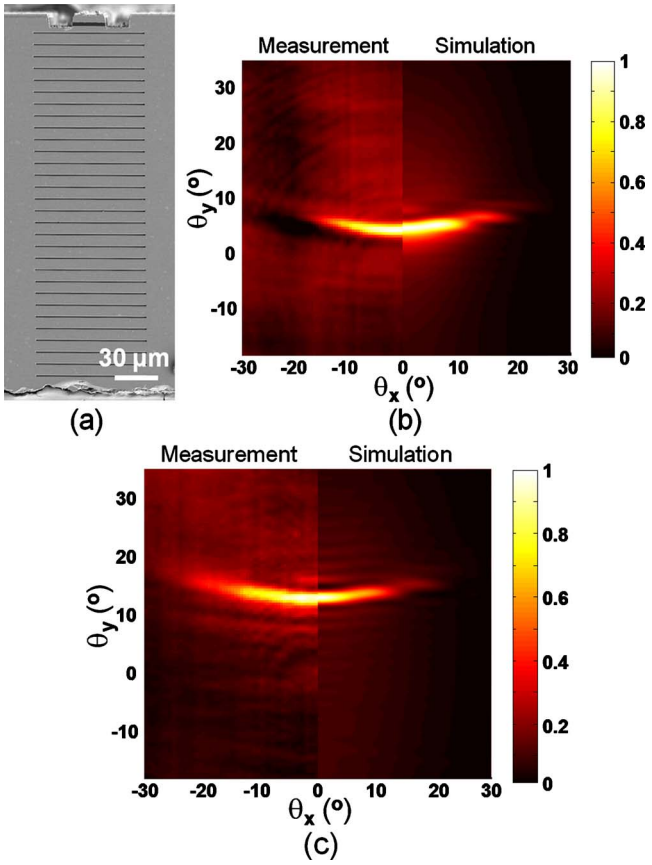

Fig. 14. (Color online) (a) SEM image of a dual-wavelength QCL patterned with a demultiplexer. (b) Measured (left half) and simulated (right half) far-field of the $\lambda_o = 9.3$ μm component of the laser emission. (c) Measured (left half) and simulated (right half) far-field of the $\lambda_o = 10.5$ μm component of the laser emission.

semiconductor lasers are mostly linearly polarized either TE or TM, which is determined by the optical selection rules of the gain medium [78,79].

We are going to discuss plasmonic structures that can create circularly polarized laser emissions [80]. But before that, we shall first see how the linearly polarized output of a QCL can be projected onto an arbitrary direction, which is a key component for achieving circular polarization. To realize linear polarization along a direction defined by θ, we use an aperture-grating structure similar to the 1D plasmonic collimator but rotated by θ from the vertical direction; see Fig. 15(a). The slit aperture is illuminated by laser waveguide modes polarized in the vertical direction. Only the component of the laser polarization perpendicular to the slit efficiently generates charge oscillations across the two edges of the slit and therefore radiates directly into the far-field and couples to SPs on the device facet. The output of the device as a result of the interference between the direct emission from the aperture and secondary emissions from the grating grooves will polarize along the θ direction.

Figure 15(a) shows SEM images of a QCL facet patterned with a linear polarizer with $\theta=45°$. Its emission divergence is reduced along the $\theta=45°$ direction (Fig. 15(b)). To determine the polarization of the emission, a mercury-cadmium-telluride-(MCT) detector with a wire-grid polarizer placed in front was positioned in the far-field where the laser intensity is maximum. As the axis of the wire-grid polarizer was rotated, the signal on the detector showed two maxima corresponding to 135° and −45° and a high cross-polarization suppression ratio (Fig. 15(c)), demonstrating the ability to efficiently project the initial vertical polarization of the laser onto the 45° direction.

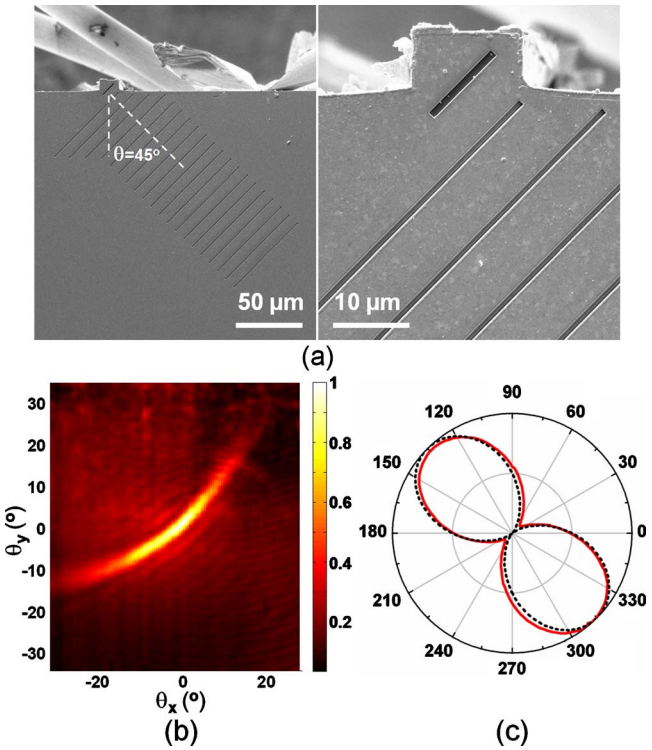

Fig. 15. (Color online) (a) SEM images of a QCL integrated with a linear polarizer. The orientation of the slit aperture and the grating grooves is 45° with respect to the vertical direction. (b) Measured emission pattern of the device in (a). (c) Measured device output as a function of the rotation angle of the wire-grid polarizer. The red solid curve is experimental data and the black dotted curve is calculation assuming a 45° linearly polarized light.

A circularly polarized beam can be constructed by coherently combining two linearly polarized beams satisfying three conditions: the two beams should have perpendicular polarizations, 90° phase difference, and the same amplitude. The first condition can be met by defining two aperture-grating structures on the device facet with their respective orientation angles equal to $\theta=\pm45°$; see Fig. 16(a). The distance between the aperture and the nearest groove, [d_1 and d_2 in Fig. 16(a)] determines the phase of the scattered light. The second condition can be satisfied

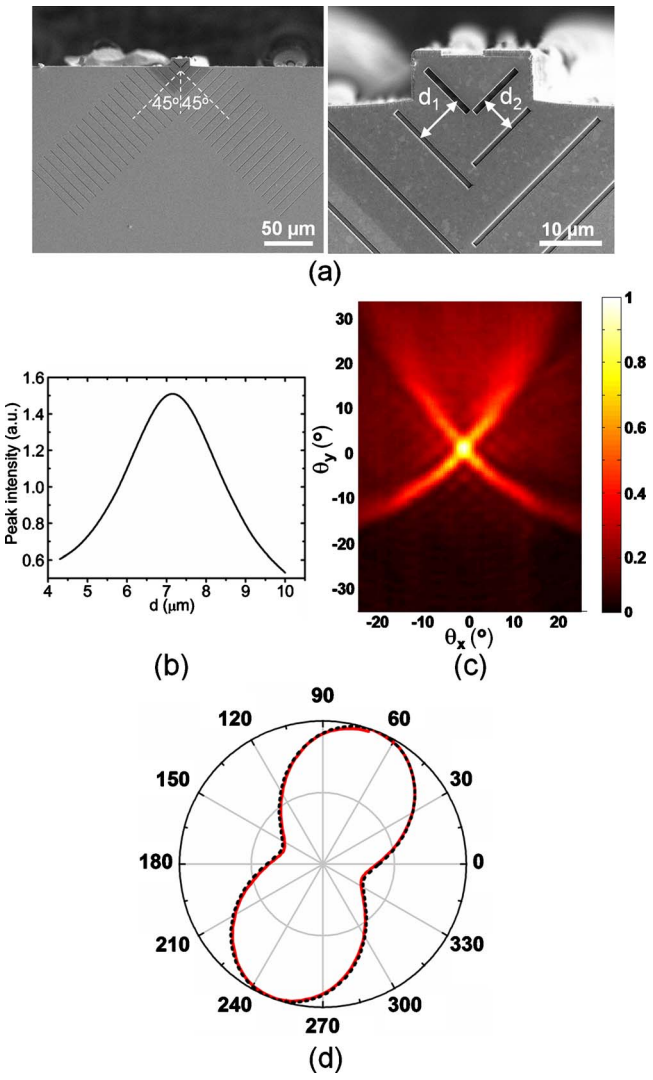

Fig. 16. (Color online) (a) SEM image of a QCL capable of producing circularly polarized emissions. (b) Calculated peak intensity of the beam created by one grating versus the distance between the aperture and the first grating groove d. Laser wavelength is assumed to be $\lambda_o=9.9$ μm. (c) Measured emission pattern of the device in (a). (d) Measured optical power of the central spot in (c) while a wire-grid polarizer was rotated in front of the detector. The red solid curve is experimental data and the black dotted curve is a fitting assuming coherent superposition of a circularly polarized component and a linearly polarized component.

by choosing $|d_1-d_2|\approx\lambda_{sp}/4$, so that the two beams produced by the left and the right gratings will have a 90° phase difference.

The efficiency of coupling laser emission into SPs on the facet is a periodic function of d, the separation between the aperture and the first grating groove. The efficiency reaches maxima when the reflected SPs by the grating and the SPs launched at the aperture and propagating towards the device top contact are out of phase. This condition translates to

$$2\pi + 2dk_{sp} = (2m+1)\pi \quad (6)$$

where the first term, 2π, is the phase picked up by SPs on reflection at the second-order grating [81]; the second term originates from path differences of the two SP components; m is an integer. Equation (6) predicts that the coupling efficiency of SPs on the facet is the highest for $d=3\lambda_{sp}/4$, which is confirmed by our simulations; see Fig. 16(b). We chose d_1 and d_2 to be respectively larger and smaller than $d=3\lambda_{sp}/4$, to satisfy the third condition for creating circular polarization, provided that $|d_1-d_2|\approx\lambda_{sp}/4$.

The device shown in Fig. 16(a) emits light that contains a circularly polarized component. Each grating on the device facet contributes to a 1D collimated beam, and the far-field pattern is cross-shaped; see Fig. 16(c). Figure 16(d) is the measured device output when a wire-grid polarizer was rotated in front of the detector, which was placed in the far-field corresponding to the center of the cross. Analysis showed that this part of the laser beam consists of a right circularly polarized component and a linearly polarized component. The former is about 1.5 times stronger than the latter in amplitude. The direct emissions from the two apertures have no phase difference and they contribute to the linearly polarized optical background.

Several strategies can be employed to boost the circularly polarized emission. By adding spoof SP grooves adjacent to the laser aperture, one can couple more light into SPs and suppress the direct emission into the far-field. Instead of using straight grating grooves, circular ones will give rise to 2D collimated light, so that the two beams coming from the left and right gratings will have better spatial overlap.

7. PLASMONIC COLLIMATORS FOR THz QCLs

A. Collimation with Plasmonic Second-Order Gratings

To address the beam quality problem of double-metal waveguide THz QCLs without compromising their high temperature performances, we first adapted a second-order grating design similar to the mid-IR collimators discussed previously.

All the grating grooves were sculpted directly on the GaAs facet without any metal coating. We take advantage of the fact that in the THz frequency range the carrier concentration in heavily doped semiconductors is sufficiently large that the semiconductor is "metallic" with the real part of its dielectric permittivity being largely negative. The Drude model was used to calculate the permittivity of GaAs [82,83], and it was found that $\epsilon_{GaAs}\approx-200+42i$ for our device and the measurement conditions ($\lambda_o=100$ μm, GaAs n-doped to 1.6×10^{18} cm^{-3}, $T=80$ K).

The limited facet area allows only five grating grooves to be defined; see Fig. 17(a). To enhance the interaction between the grating and the loosely confined THz SPs, we used fairly large grating grooves (depth and width ~15%–20% of λ_o) so that the energy of the SPs can be scattered into the far-field as efficiently as possible. The

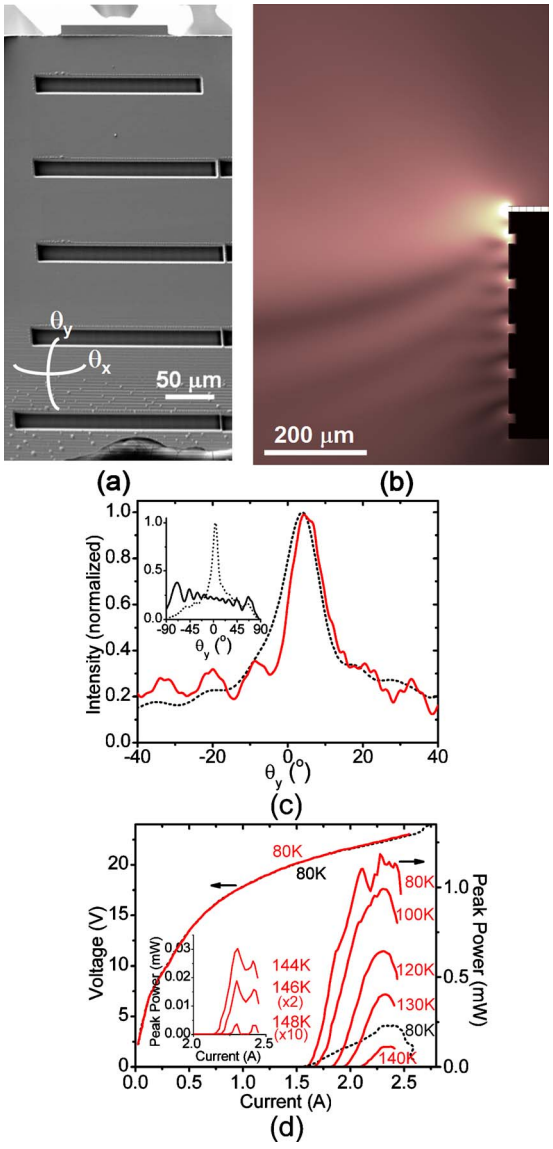

Fig. 17. (Color online) (a) SEM image of a $\lambda_o=100$ THz QCL with second-order grating grooves directly sculpted into the GaAs facet. The grating has groove width and depth of 18 μm and 14 μm, respectively, and has periodicity of 88 μm. The center-to-center distance between the laser aperture and the nearest groove is 58 μm. (b) Simulated electric-field distribution ($|E|$) of the device. (c) The red solid curve and black dotted curve are measured and calculated vertical far-field of the device, respectively. Insets show calculated vertical far-field of the original (solid curve) and the collimated (dotted curve) devices in the half space. (c) LIV characteristics and temperature performances of the device before (black dotted curves) and after (red solid curves) defining the collimator.

effects of the second-order grating on the dispersion of SPs are illustrated by the improved SP confinement; see Fig. 17(b).

Experimental results for one representative device are shown in Figs. 17(c) and 17(d). The measured vertical far-field emission profile of the device agrees reasonably well with calculations. The FWHM divergence angle is about 15° (Fig. 17(c)). Thanks to the improved emission profile, the collected power of the device increases by a factor of ~5 compared to the original unpatterned device at 80 K (Fig. 17(d)).

B. Collimators Based on Metasurfaces

In the previous example the far-field shows a fairly large optical background approaching 30% of the peak intensity of the central lobe, and this is due to the dominance of the direct emission from the laser aperture over the secondary emissions from the grating grooves. The latter are comparatively weak because of the inefficient coupling into SPs. It is estimated, according to simulations, that the optical power coupled into SPs confined to the laser facet is merely 15%, while the remaining 85% is radiated directly into the far-field.

An improved design involves adding spoof SP grooves adjacent to the laser aperture and between the second-order grating grooves, forming a "metasurface" collimator. A schematic of the design for a ~3.19 THz (λ_o=94 μm) laser and its cross-section are shown in Figs. 18(a) and 18(b), respectively. Two colors are used in the figures to identify the second-order grating (pink) and the spoof SPP grooves (blue). Metasurfaces are an extension of the concept of metamaterials to planar optics where the dispersion properties of SPs are spatially tailored by structuring metallic surfaces. Metasurfaces or metafilms have been under rapid progress in recent years and have found interesting applications such as subwavelength imaging [84], waveguiding [85,86], and the localization [85,86], confinement [87], and slowing of light [88].

In the original unpatterned device, the laser emits both directly into the far-field and into Zenneck waves on the facet; both components have a wavevector close to k_o. The wavevector of the laser mode in the waveguide is several times larger, $n_{eff}k_o$ (n_{eff}≈3.5 is the effective mode index). So there is a wavevector mismatch of the modes at the aperture. In our collimator, the spoof SP grooves adjacent to the aperture increase the effective in-plane wavevector of the SPs, reducing the wavevector mismatch. More light is therefore coupled out from the laser cavity, and a larger percentage of it is channeled into SPs on the facet instead of being directly emitted into the far-field. Most importantly, the spoof SP grooves greatly increase the confinement of SPs, thus improving the scattering efficiency of the second-order grating grooves. Constructive interference between the scattered waves and the direct emission from the laser aperture gives rise to a low-divergence beam normal to the facet in the far-field.

Figure 18(c) shows that the in-plane wavevector increases by ~25% for the grooves adjacent to the laser aperture (red dash-double-dotted curve). The depth of the spoof SP grooves was chosen to be in the range 6–11 μm to provide sufficient confinement without introducing large optical losses, which are mainly due to Ohmic absorption and rise sharply as d increases [89]. Figure 18(d) shows that the confinement of SPs is improved to a few tens of micrometers, representing a reduction in decay length by approximately one order of magnitude compared to Zenneck waves on a planar GaAs interface (~300 μm).

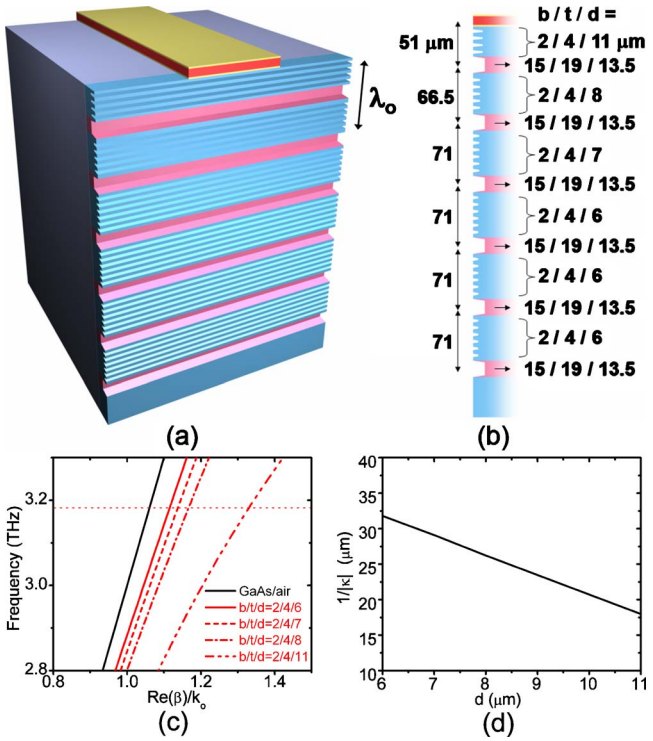

Fig. 18. (Color online) (a) Schematic of a THz QCL integrated with a metasurface collimator. (b) Cross-section of the design for a λ_o=94 μm device. The width of the bottom and top of the grooves, and groove depth are labeled as b, t, and d, respectively. The periodicity of the spoof SP grooves is 8 μm. (c) The black curve is the dispersion diagram of SPs on a planar semiconductor/air interface, which is very close to the light line. The red curves are the dispersion diagrams corresponding to the different sections of the spoof SP structures. The horizontal dotted line indicates the laser frequency. (d) 1/e decay length of the spoof SP electric field (|E|) normal to the interface into the air as a function of d.

The simulated electric-field distribution (|E|) of the device is presented in Fig. 19(a). Waves scattered from the laser facet by the collimator are clearly observed in the near- and meso-field, and confined SPs can be seen on the facet. Simulations indicate that, compared to the original unpatterned device, the power throughput of the collimated device is increased by approximately 25%. In addition, it is estimated that about half of the laser output is coupled into SP modes on the facet while the remaining half is emitted directly into the far-field. As a result of a more uniform energy distribution in the near-field, the far-field of the device with the metasurface collimator should have much higher directivity.

Figure 19(b) shows an SEM image of the facet of a device fabricated using FIB milling. The collimator occupies a small footprint with dimensions ~$4\lambda_o \times 4.5\lambda_o$. The central beam has vertical and lateral FWHM divergence angles of ~11° and ~19°, respectively (Fig. 19(c)); the optical background has average intensity below 10% of the

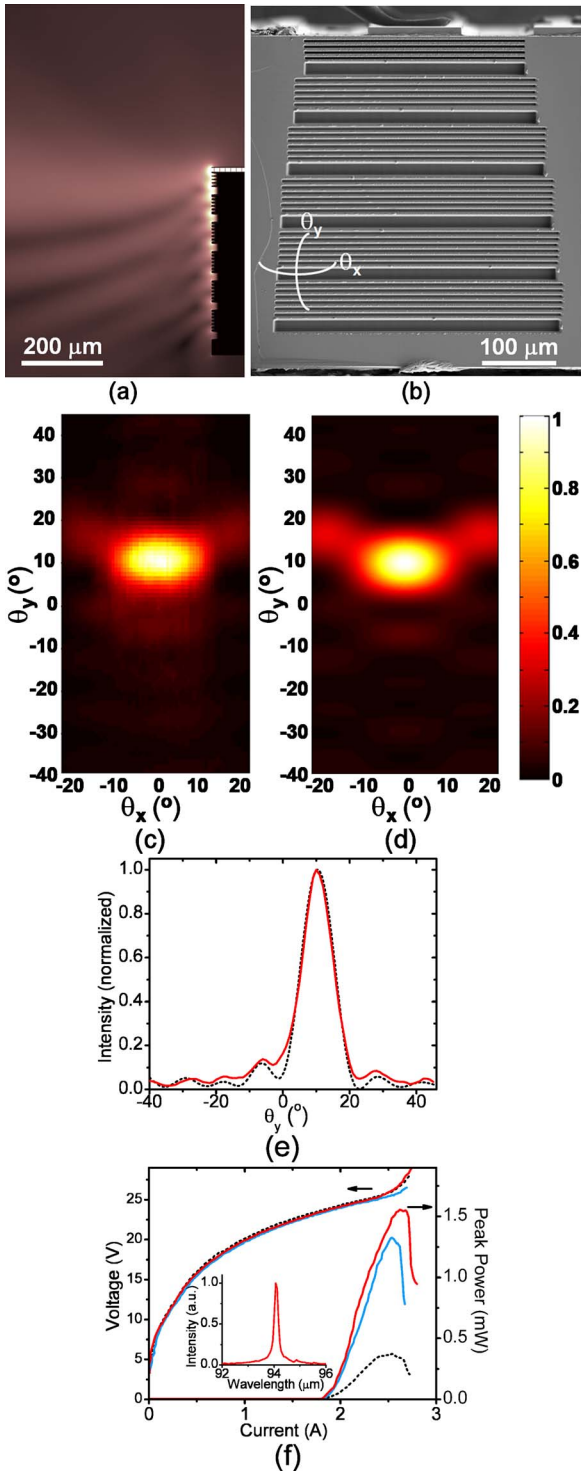

Fig. 19. (Color online) (a) Simulated electric-field distribution ($|E|$) of the device with a metasurface collimator. (b) SEM image of a device fabricated according to the design in Fig. 18. (c) and (d) Measured and simulated emission patterns of the device. (e) Vertical line-scans of (c) (red solid curve) and (d) (black dotted curve) along $\theta_x = 0°$. (f) LIV characteristics of the device. The black, blue, and red curves are for the unpatterned device, the device with only the second-order grating and the device with the metasurface collimator, respectively. Inset: spectrum of the collimated device measured at $I = 2.5$ A.

central lobe peak intensity (Fig. 19(e)). All are in good agreement with the 3D full-wave simulation results in Figs. 19(d) and 19(e). The beam quality of our collimated device is better than or comparable to those obtained in THz QCLs with higher-order gratings, photonic crystals, or mounted micro optical elements [35,36,44–46,48]. The small divergence beam emitted from our THz device is compatible with the receiver front end of modern submillimeter heterodyne detection systems [90,91].

The collected power of the collimated device increases by a factor of ~4.5 compared to the original unpatterned device (Fig. 19(f)). The enhancement factor is ~3.7 for the device with only the second-order grating. This difference in measured power is primarily a result of the increased total power throughput originating from the reduced wavevector mismatch in the metasurface collimator. Our power measurement apparatus with a collection cone of ~50° captures the main lobe as well as a significant portion of the background light. Eventually what matters in applications is the power carried in the main lobe of a laser beam, because the optical background is often lost during propagation in optical systems. Based on the far-field measurements, the power in the main lobe of the device with the metasurface collimator is about two times larger than that of the device with the second-order grating. Figure 19(f) shows that the maximum operating temperature of the patterned device is 140 K, the same as that of the original device, and that the lasing threshold does not change after defining the collimator.

We can go one step further to create a metasurface collimator consisting entirely of spoof SP structures [92]; see Fig. 20(a). Spoof SP grooves with different depths periodically modulate the SP dispersion, creating an effective second-order grating that couples the energy of the SPs into the far-field (Fig. 20(c)). The grooves adjacent to the laser aperture help increase device power throughput by coupling more laser output into spoof SPs on the facet; the shallow "blue" grooves contribute to SP confinement.

The fabricated device shows very similar performances as the previous one; see Fig. 21. The central beam has vertical and lateral FWHM divergence angles of ~12° and ~16°, respectively; the optical background is below 10% of the peak intensity. The measured beam directivity is increased from ~5 dB for the original unpatterned laser, to ~11 dB for the device with only the deep "pink" spoof SP grooves, and to ~16 dB for the device with the complete structure. The power collection efficiency is enhanced by a factor of ~6.

C. Reducing Lateral Far-Field Divergence by Utilizing Channel Polaritons

In the two metasurface-based QCLs shown above, reduction of beam divergence occurs in both the vertical and lateral directions. In the vertical direction, it is owing to an antenna array effect. In the lateral direction, it is due to an increased effective emission area: the metasurface patterns were intentionally fabricated to be a few times wider than the laser waveguide (see SEM images in Figs. 19 and 21), which helps spread SPs laterally. As such, 2D collimation was realized using 1D structures composed of straight grooves; this is different from ring-shaped 2D plasmonic collimators for mid-IR QCLs in Section 4.

Figure 22(a) shows simulated near-field distribution of the device in Fig. 21. As a comparison, Fig. 22(c) shows

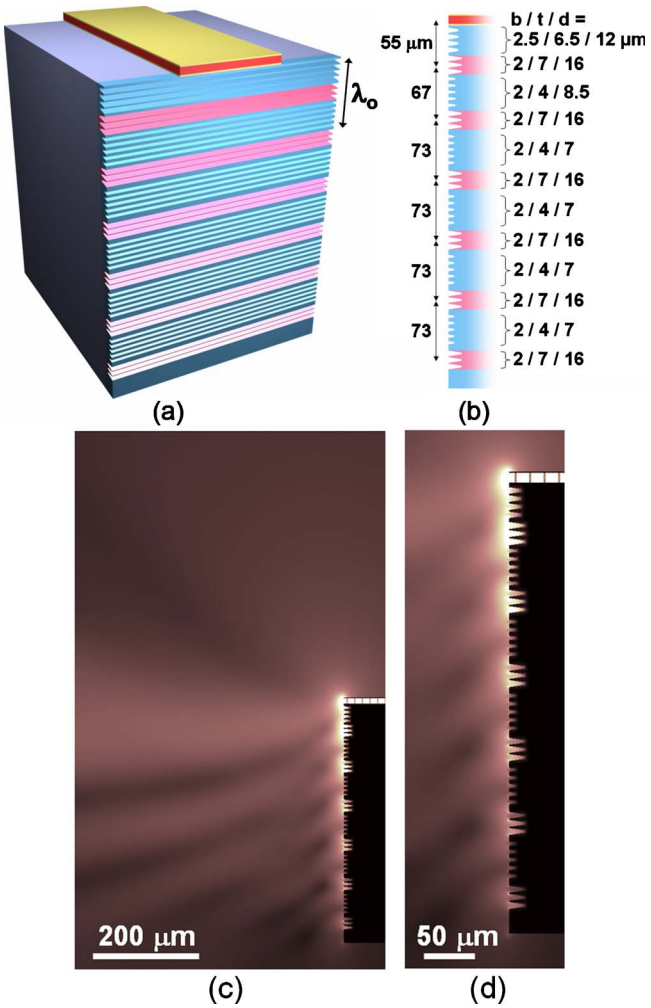

Fig. 20. (Color online) (a) Schematic of a THz QCL patterned with a metasurface collimator consisting entirely of spoof SP grooves. (b) Cross-section of the design for a $\lambda_o = 100$ μm device. The periodicity of the spoof SP grooves is 8 μm. (c) Simulated electric-field distribution ($|E|$) of the device. (d) Zoom-in view of (c) showing the confined SPs on the device facet.

the result of another device with the same design except that the metasurface pattern is much narrower. As a result of the difference in lateral dimension of the near-field, the far-field emission profiles of the two devices are markedly different: the former has a much smaller lateral beam divergence; compare Figs. 22(b) and 22(d).

The lateral spreading is so efficient that SPs are observed to reach the side boundaries of the plasmonic pattern within the first few grooves adjacent to the laser aperture; see Fig. 22(a). Physically, laser emission first excites the central section of the long spoof SP grooves; the channel polariton modes generated then propagate along the grooves in a way analogous to TEM waves traveling along coplanar strip transmission lines. As discussed in section 2, deeper grooves support channel polaritons that are more confined with less leakage out of the grooves; therefore the polariton modes are able to propagate longer distances, leading to more efficient lateral spreading. This is confirmed by simulations of a laser facet sculpted with periodic spoof SP grooves. Figure 23 shows that for deeper grooves the lateral spreading of SPs

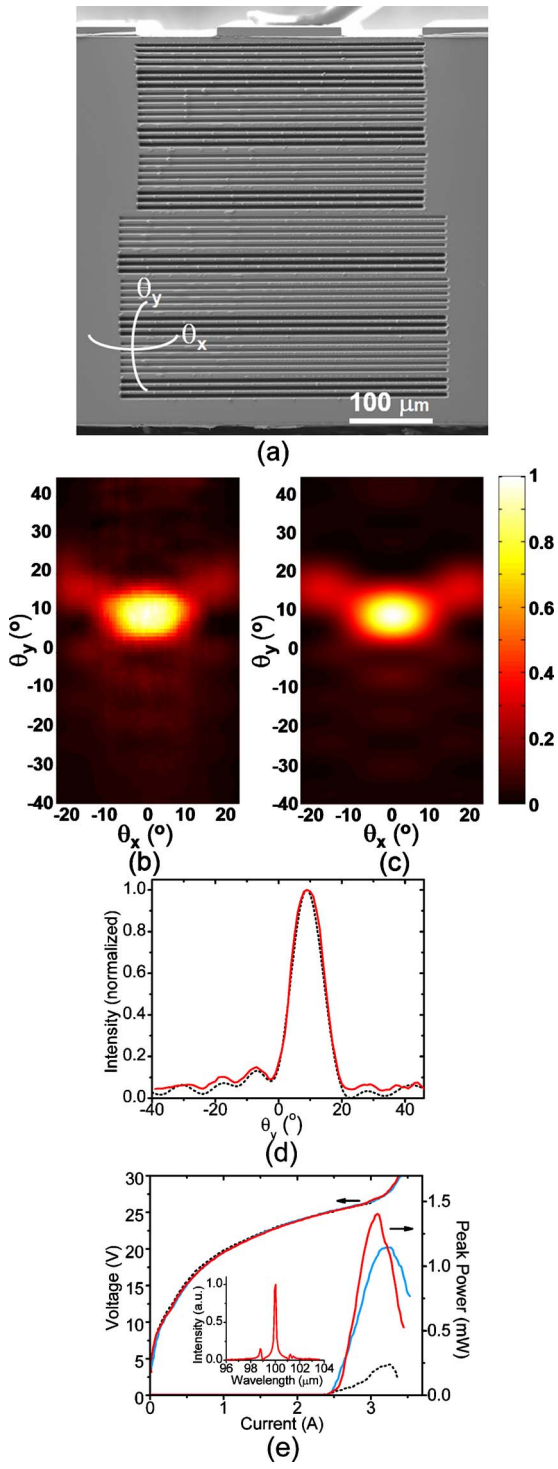

Fig. 21. (Color online) (a) SEM image of a $\lambda_o = 100$ μm QCL fabricated according to the design in Fig. 20. (b) and (c) Measured and simulated emission profiles of the device. (d) Line-scans of (b) (red solid curve) and (c) (black dotted curve) along $\theta_x = 0°$. (e) LIV characteristics of the device. The black, blue, and red curves are for the unpatterned device, the device with only the deep spoof SP grooves and the device with the complete structure, respectively.

on the facet is wider and the near-fields are more intensive and uniform.

The channel polariton scheme can also be applied to mid-IR QCLs to efficiently reduce lateral beam diver-

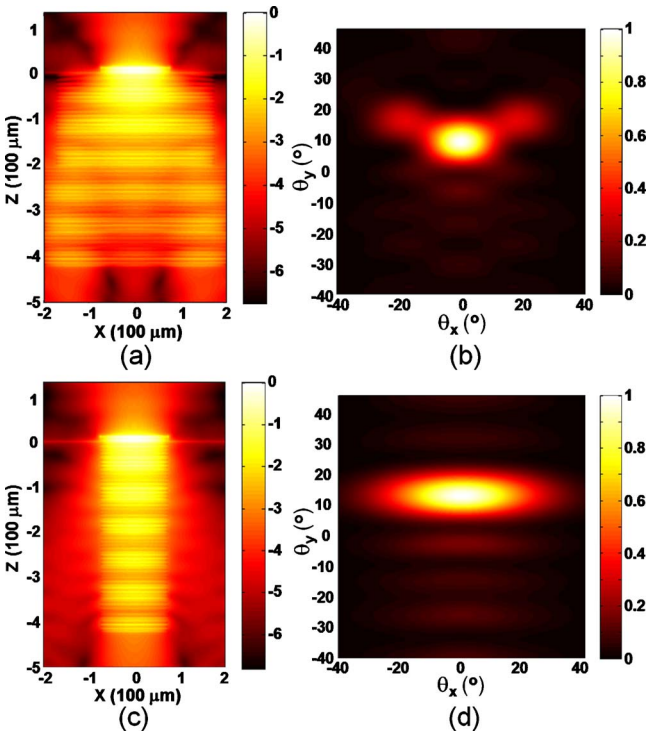

Fig. 22. (Color online) (a) Simulated near-field distribution ($log_e(|E|/max(|E|))$) of the device shown in Fig. 21. The near-field is monitored on a plane 1 μm above the device facet. (b) Simulated far-field corresponding to (a). (c) Simulated near-field distribution of another device with a narrower metasurface pattern. The pattern is ~400 μm wide in (a) but only 150 μm wide in (c), which is equal to the width of the laser waveguide. (d) Simulated far-field corresponding to (c).

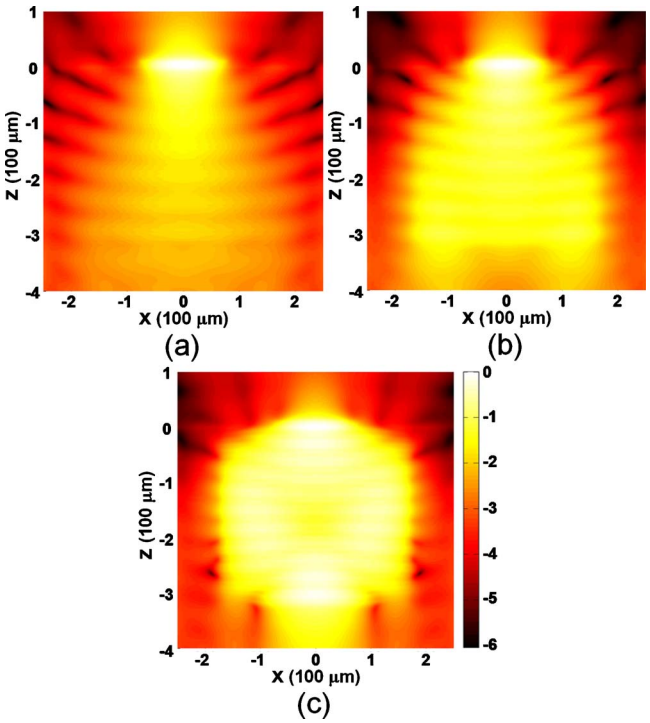

Fig. 23. (Color online) Simulated near-field intensity distributions ($log_{10}(|E|^2/max(|E|^2))$) on device facets sculpted with spoof SP grooves with different depth: 5, 12, and 16 μm for (a), (b), and (c), respectively. The three structures have the same groove width of 4 μm (measured along the vertical direction), periodicity of 8 μm, and length of 350 μm (measured along the lateral direction). The near-field is monitored on a plane 5 μm above the device facet. Laser wavelength is $\lambda_o = 100$ μm.

gence. The advantage compared to the ring-shaped 2D collimators discussed in section 4 is that one does not need subwavelength apertures for lateral spreading of SPs. 2D collimation with high power throughput can be achieved by using a 1D design with widely open apertures.

8. CONCLUSIONS AND FUTURE PERSPECTIVES

We have demonstrated that, by monolithically integrating on the emission facet of mid-IR and THz QCLs, properly designed plasmonic structures that tailor the dispersion properties of surface plasmons, the device performance can be significantly enhanced and new functionalities can be realized.

Future interesting direction in wavefront engineering with plasmonics includes creating light sources capable of producing special beams such as Bessel beams [93], which are diffraction free, beams that are radially or azimuthally polarized [94], and beams with orbital angular momentum [95,96], which can be used to rotate small dielectric particles.

In this paper we discussed only wavefront engineering of light sources in the far-field, but the possibilities that plasmonics can offer in near-field engineering are also enormous starting from resonant optical antennas and antenna arrays [97,98]. Antenna structures can be integrated on optical components such as semiconductor lasers and optical fibers. By properly engineering the extinction spectra and/or the scattering cross sections of the antenna structures, one can create near-field optical devices with applications ranging from high-resolution probes for imaging/spectroscopy [99,100], to broadband lenses for solar cells [101,102], and novel modulators/detectors/sensors [103].

We further envision using soft-lithography based techniques for inexpensive, high-throughput fabrication of plasmonic structures so that we are not restricted to focused-ion beam milling, which is mostly suitable for proof-of-concept demonstrations. We have seen encouraging progress in this direction in the past few years. For example, nanoskiving [104] in combination with replica molding [105] has been developed as a simple and convenient procedure to produce arrays of single- or multicomponent metallic structures with deep-subwavelength features and high aspect ratio [106]. A soft-lithography based pattern transfer technique “decal transfer” [107] has been developed for convenient and reliable fabrication of plasmonic structures on the facet of optical devices.

ACKNOWLEDGMENTS

We gratefully acknowledge the following people who contributed to the work presented in this paper: R. Blanchard, M. A. Kats, J. A. Fan, Q. J. Wang, C. Pflügl, L. Diehl, M. A. Belkin, S. P. Khanna, L. Li, A. G. Davies, E. H. Linfield, T. Edamura, S. Furuta, M. Yamanishi, H.

Kan, M. Geiser, M. Fischer, A. Wittmann, J. Faist, and N. Antoniou. We acknowledge funding from U.S. Air Force Office of Scientific Reserach (AFOSR) under contract No. FA9550-09-0505-DOD, the Engineering and Physical Sciences Research Council (EPSRC) (UK), and Hamamatsu Photonics (Japan). The authors acknowledge support from the National Science Foundation, Harvard Nanoscale Science and Engineering Center (NSEC), and the Center for Nanoscale Systems (CNS) at Harvard University. Harvard CNS is a member of the National Nanotechnology Infrastructure Network (NNIN). Some of the computations in this paper were run on the Odyssey cluster supported by the Harvard Faculty of Arts and Sciences (FAS) Sciences Division Research Computing Group.

REFERENCES

1. R. F. Kazarinov and R. A. Suris, "Amplification of electromagnetic waves in a semiconductor superlattice," Sov. Phys. Semicond. **5**, 707–709 (1971).
2. J. Faist, F. Capasso, D. L. Sivco, A. L. Hutchinson, and A. Y. Cho, "Quantum cascade laser," Science **264**, 553–556 (1994).
3. C. Gmachl, F. Capasso, D. L. Sivco, and A. Y. Cho, "Recent progress in quantum cascade lasers and applications," Rep. Prog. Phys. **64**, 1533–1601 (2001).
4. F. Capasso, C. Gmachl, R. Paiella, A. Tredicucci, A. L. Hutchinson, D. L. Sivco, J. N. Baillargeon, A. Y. Cho, and H. C. Liu, "New frontiers in quantum cascade lasers and applications," IEEE J. Sel. Top. Quantum Electron. **6**, 931–947 (2000).
5. M. Beck, D. Hofstetter, T. Aellen, J. Faist, U. Oesterle, M. Ilegems, E. Gini, and H. Melchior, "Continuous wave operation of a mid-infrared semiconductor laser at room temperature," Science **295**, 301–305 (2002).
6. Y. Bai, S. Slivken, S. R. Darvish, A. Haddadi, B. Gokden, and M. Razeghi, "High power broad area quantum cascade lasers," Appl. Phys. Lett. **95**, 221104 (2009).
7. M. Razeghi, "High-power high-wall plug efficiency mid-infrared quantum cascade lasers based on InP/GaInAs/InAlAs material system," Proc. SPIE **7230**, 723011 (2009).
8. A. Lyakh, R. Maulini, A. Tsekoun, R. Go, C. Pflügl, L. Diehl, Q. J. Wang, F. Capasso, and C. K. N. Patel, "3 W continuous-wave room temperature single-facet emission from quantum cascade lasers based on nonresonant extraction design approach," Appl. Phys. Lett. **95**, 141113 (2009).
9. J. Faist, C. Gmachl, F. Capasso, C. Sirtori, D. L. Sivco, J. N. Baillargeon, A. L. Hutchinson, and A. Y. Cho, "Distributed feedback quantum cascade lasers," Appl. Phys. Lett. **70**, 2670–2672 (1997).
10. C. Gmachl, J. Faist, J. N. Baillargeon, F. Capasso, C. Sirtori, D. L. Sivco, S. N. G. Chu, and A. Y. Cho, "Complex-coupled quantum cascade distributed-feedback laser," IEEE Photonics Technol. Lett. **9**, 1090–1092 (1997).
11. G. Wysocki, R. F. Curl, F. K. Tittel, R. Maulini, J. M. Bulliard, and J. Faist, "Widely tunable mode-hop free external cavity quantum cascade laser for high resolution spectroscopic applications," Appl. Phys. B **81**, 769–777 (2005).
12. R. Maulini, A. Mohan, M. Giovannini, J. Faist, and E. Gini, "External cavity quantum-cascade laser tunable from 8.2 to 10.4 μm using a gain element with a heterogeneous cascade," Appl. Phys. Lett. **88**, 201113 (2006).
13. M. B. Pushkarsky, I. G. Dunayevskiy, M. Prasanna, A. G. Tsekoun, R. Go, and C. K. N. Patel, "High-sensitivity detection of TNT," Proc. Natl. Acad. Sci. U.S.A. **103**, 19630–19634 (2006).
14. M. Pushkarsky, A. Tsekoun, I. G. Dunayevskiy, R. Go, and C. K. N. Patel, "Sub-parts-per-billion level detection of NO2 using room-temperature quantum cascade lasers," Proc. Natl. Acad. Sci. U.S.A. **103**, 10846–10849 (2006).
15. G. Wysocki, R. Lewicki, R. F. Curl, F. K. Tittel, L. Diehl, F. Capasso, M. Troccoli, G. Hofler, D. Bour, S. Corzine, R. Maulini, M. Giovannini, and J. Faist, "Widely tunable mode-hop free external cavity quantum cascade lasers for high resolution spectroscopy and chemical sensing," Appl. Phys. B **92**, 305–311 (2008).
16. A. Wittmann, A. Hugi, E. Gini, N. Hoyler, and J. Faist, "Heterogeneous high-performance quantum-cascade laser sources for broad-band tuning," IEEE J. Quantum Electron. **44**, 1083–1088 (2008).
17. A. Hugi, R. Terazzi, Y. Bonetti, A. Wittmann, M. Fischer, M. Beck, J. Faist, and E. Gini, "External cavity quantum cascade laser tunable from 7.6 to 11.4 μm," Appl. Phys. Lett. **95**, 061103 (2009).
18. B. G. Lee, M. A. Belkin, R. Audet, J. MacArthur, L. Diehl, C. Pflügl, F. Capasso, D. C. Oakley, D. Chapman, A. Napoleone, D. Bour, S. Corzine, G. Höfler, and J. Faist, "Widely tunable single-mode quantum cascade laser source for mid-infrared spectroscopy," Appl. Phys. Lett. **91**, 231101 (2007).
19. B. G. Lee, H. A. Zhang, C. Pflügl, L. Diehl, M. A. Belkin, M. Fischer, A. Wittmann, J. Faist, and F. Capasso, "Broadband distributed-feedback quantum cascade laser array operating from 8.0 to 9.8 μm," IEEE Photonics Technol. Lett. **21**, 914–916 (2009).
20. M. Troccoli, L. Diehl, D. P. Bour, S. W. Corzine, N. Yu, C. Y. Wang, M. A. Belkin, G. Hofler, R. Lewicki, G. Wysocki, F. K. Tittel, and F. Capasso, "High-performance quantum cascade lasers grown by metal-organic vapor phase epitaxy and their applications to trace gas sensing," J. Lightwave Technol. **26**, 3534–3555 (2008).
21. A. Lyakh, C. Pflügl, L. Diehl, Q. J. Wang, F. Capasso, X. J. Wang, J. Y. Fan, T. Tanbun-Ek, R. Maulini, A. Tsekoun, R. Go, and C. K. N. Patel, "1.6 W high wall plug efficiency, continuous-wave room temperature quantum cascade laser emitting at 4.6 μm," Appl. Phys. Lett. **92**, 111110 (2008).
22. R. Köhler, A. Tredicucci, F. Beltram, H. E. Beere, E. H. Linfield, A. G. Davies, D. A. Ritchie, R. C. Iotti, and F. Rossi, "Terahertz semiconductor-heterostructure laser," Nature **417**, 156–159 (2002).
23. B. S. Williams, "Terahertz quantum-cascade lasers," Nat. Photonics **1**, 517–525 (2007).
24. G. Scalari, C. Walther, M. Fischer, R. Terazzi, H. Beere, D. Ritchie, and J. Faist, "THz and sub-THz quantum cascade lasers," Laser Photonics Rev. **1**, 1–22 (2008).
25. M. A. Belkin, Q. J. Wang, C. Pflügl, A. Belyanin, S. P. Khanna, A. G. Davies, E. H. Linfield, and F. Capasso, "High-temperature operation of terahertz quantum cascade laser sources," IEEE J. Sel. Top. Quantum Electron. **15**, 952–967 (2009).
26. A. W. M. Lee, Q. Qin, S. Kumar, B. S. Williams, Qing Hu, and J. L. Reno, "Real-time terahertz imaging over a standoff distance (>25 meters)," Appl. Phys. Lett. **89**, 141125 (2006).
27. J. Faist, G. Scalari, C. Walther, and M. Fischer, "Progress in long wavelength terahertz quantum cascade lasers," presented at the 2007 Materials Research Society (MRS) Spring Meeting, San Francisco, California, April 9–13, 2007, paper CC7.2.
28. S. Kumar, Q. Hu, and J. L. Reno, "186 K operation of terahertz quantum-cascade lasers based on a diagonal design," Appl. Phys. Lett. **94**, 131105 (2009).
29. B. S. Williams, S. Kumar, Q. Hu, and J. L. Reno, "Operation of terahertz quantum-cascade lasers at 164 K in pulsed mode and at 117 K in continuous-wave mode," Opt. Express **13**, 3331–3339 (2005).
30. B. S. Williams, S. Kumar, Q. Hu, and J. L. Reno, "High-power terahertz quantum cascade lasers," Electron. Lett. **42**, 89–91 (2006).
31. R. H. Rediker, I. Melngailis, and A. Mooradian, "Lasers, their development, and applications at M.I.T. Lincoln Laboratory," IEEE J. Quantum Electron. **20**, 602–615 (1984).
32. S. Mukherjee and Z. S. Shi, "State-of-the-art IV–VI semiconductor light-emitting devices in mid-infrared optoelectronic applications," IETE Tech. Rev. **26**, 236–246 (2009).

33. S. Kohen, B. S. Williams, and Q. Hu, "Electromagnetic modeling of terahertz quantum cascade laser waveguides and resonators," J. Appl. Phys. **97**, 053106 (2005).
34. M. Hajenius, P. Khosropanah, J. N. Novenier, J. R. Gao, T. M. Klapwijk, S. Barbieri, S. Dhillon, P. Filloux, C. Sirtori, D. A. Ritchie, and H. E. Beere, "Surface plasmon quantum cascade lasers as terahertz local oscillators," Opt. Lett. **33**, 312–314 (2008).
35. A. W. M. Lee, Q. Qin, S. Kumar, B. S. Williams, Q. Hu, and J. L. Reno, "High-power and high-temperature THz quantum-cascade lasers based on lens-coupled metal-metal waveguides," Opt. Lett. **32**, 2840–2842 (2007).
36. M. I. Amanti, M. Fischer, C. Walther, G. Scalari, and J. Faist, "Horn antennas for terahertz quantum cascade lasers," Electron. Lett. **43**, 573–574 (2007).
37. M. Troccoli, C. Gmachl, F. Capasso, D. L. Sivco, and A. Y. Cho, "Mid-infrared ($\lambda \approx 7.4$ μm) quantum cascade laser amplifier for high-power single-mode emission and improved beam quality," Appl. Phys. Lett. **80**, 4103–4105 (2002).
38. L. Nähle, J. Semmel, W. Kaiser, S. Höfling, and A. Forchel, "Tapered quantum cascade lasers," Appl. Phys. Lett. **91**, 181122 (2007).
39. Y. Bai, S. R. Darvish, S. Slivken, P. Sung, J. Nguyen, A. Evans, W. Zhang, and M. Razeghi, "Electrically pumped photonic crystal distributed feedback quantum cascade lasers," Appl. Phys. Lett. **91**, 141123 (2007).
40. D. Hofstetter, J. Faist, M. Beck, and U. Oesterle, "Surface-emitting 10.1 μm quantum-cascade distributed feedback lasers," Appl. Phys. Lett. **75**, 3769–3771 (1999).
41. W. Schrenk, N. Finger, S. Gianordoli, L. Hvozdara, G. Strasser, and E. Gornik, "Surface-emitting distributed feedback quantum-cascade lasers," Appl. Phys. Lett. **77**, 2086–2088 (2000).
42. D. Hofstetter, J. Faist, M. Beck, A. Müller, and U. Oesterle, "Edge- and surface-emitting 10.1 μm quantum cascade distributed feedback lasers," Physica E **7**, 25–28 (2000).
43. C. Pflügl, M. Austerer, W. Schrenk, S. Golka, G. Strasser, R. P. Green, L. R. Wilson, J. W. Cockburn, A. B. Krysa, and J. S. Roberts, "Single-mode surface-emitting quantum-cascade lasers," Appl. Phys. Lett. **86**, 211101 (2005).
44. J. A. Fan, M. A. Belkin, and F. Capasso, "Surface emitting terahertz quantum cascade laser with a double-metal waveguide," Opt. Express **14**, 11672–11680 (2006).
45. S. Kumar, B. S. Williams, Q. Qin, A. W. M. Lee, and Q. Hu, "Surface-emitting distributed feedback terahertz quantum-cascade lasers in metal-metal waveguides," Opt. Express **15**, 114–128 (2007).
46. M. I. Amanti, M. Fischer, G. Scalari, M. Beck and J. Faist, "Low-divergence single-mode terahertz quantum cascade laser," Nat. Photonics **3**, 586–590 (2009).
47. E. Mujagić, L. K. Hoffmann, S. Schartner, M. Nobile, W. Schrenk, M. P. Semtsiv, M. Wienold, W. T. Masselink, and G. Strasser, "Low divergence single-mode surface emitting quantum cascade ring lasers," Appl. Phys. Lett. **93**, 161101 (2008).
48. L. Mahler, A. Tredicucci, F. Beltram, C. Walther, J. Faist, B. Witzigmann, H. E. Beere, and D. A. Ritchie, "Vertically emitting microdisk lasers," Nat. Photonics **3**, 46–49 (2009).
49. I. Vurgaftman and J. R. Meyer, "Photonic-crystal distributed-feedback quantum cascade lasers," IEEE J. Quantum Electron. **38**, 592–602 (2002).
50. R. Colombelli, K. Srinivasan, M. Troccoli, O. Painter, C. F. Gmachl, D. M. Tennant, A. M. Sergent, D. L. Sivco, A. Y. Cho, and F. Capasso, "Quantum cascade surface-emitting photonic crystal laser," Science **302**, 1374–1377 (2003).
51. Y. Chassagneux, R. Colombelli, W. Maineult, S. Barbieri, H. E. Beere, D. A. Ritchie, S. P. Khanna, E. H. Linfield, and A. G. Davies, "Electrically pumped photonic-crystal terahertz lasers controlled by boundary conditions," Nature **457**, 174–178 (2009).
52. Q.-Y. Lu, W.-H. Guo, W. Zhang, L.-J. Wang, J.-Q. Liu, L.- Li, F.-Q. Liu, and Z.-G. Wang, "Room temperature operation of photonic-crystal distributed-feedback quantum cascade lasers with single longitudinal and lateral mode performance," Appl. Phys. Lett. **96**, 051112 (2010).
53. H. A. Atwater, "The promise of plasmonics," Sci. Am. **296**, 56–63 (2007).
54. E. Ozbay, "Plasmonics: merging photonics and electronics at nanoscale dimensions," Science **311**, 189–193 (2006).
55. S. A. Maier, *Plasmonics: Fundamentals and Applications* (Springer-Verlag, 2007).
56. G. Mie, "Beiträge zur Optik trüber Medien, speziell kolloidaler Metallösungen," Ann. Phys. (Leipzig) **330**, 377–445 (1908).
57. J. Zenneck, "Über die Fortpflanzung ebener elektromagnetischer Wellen längs einer ebenen Leiterfläche und ihre Beziehung zur drahtlosen Telegraphie," Ann. Phys. **23**, 846–866 (1907).
58. A. Sommerfeld, "Über die Ausbreitung der Wellen in der drahtlosen Telegraphie," Ann. Phys. **28**, 665–736 (1909).
59. S. C. Kitson, W. L. Barnes, and J. R. Sambles, "Full photonic band gap for surface modes in the visible," Phys. Rev. Lett. **77**, 2670–2673 (1996).
60. J. B. Pendry, L. Martín-Moreno, and F. J. García-Vidal, "Mimicking surface plasmons with structured surfaces," Science **305**, 847–848 (2004).
61. F. J. García-Vidal, L. Martín-Moreno, and J. B. Pendry, "Surfaces with holes in them: new plasmonic metamaterials," J. Opt. A, Pure Appl. Opt. **7**, S97–S101 (2005).
62. C. R. Williams, S. R. Andrews, S. A. Maier, A. I. Fernández-Domínguez, L. Martín-Moreno, and F. J. García-Vidal, "Highly confined guiding of terahertz surface plasmon polaritons on structured metal surfaces," Nat. Photonics **2**, 175–179 (2008).
63. J. A. Kong, *Electromagnetic Wave Theory* (EMW Publishing, 2000).
64. J. Q. Lu and A. A. Maradudin, "Channel plasmons," Phys. Rev. B **42**, 11159–11165 (1990).
65. I. V. Novikov and A. A. Maradudin, "Channel polaritons," Phys. Rev. B **66**, 035403 (2002).
66. D. K. Gramotnev and D. F. P. Pile, "Single-mode subwavelength waveguide with channel plasmon-polaritons in triangular grooves on a metal surface," Appl. Phys. Lett. **85**, 6323–6325 (2004).
67. S. I. Bozhevolnyi, V. S. Volkov, E. Devaux, J.-Y. Laluet, and T. W. Ebbesen, "Channel plasmon subwavelength waveguide components including interferometers and ring resonators," Nature **440**, 508–511 (2006).
68. S. I. Bozhevolnyi, V. S. Volkov, E. Devaux, and T. W. Ebbesen, "Channel plasmon-polariton guiding by subwavelength metal grooves," Phys. Rev. Lett. **95**, 046802 (2005).
69. S. I. Bozhevolnyi, "Effective-index modeling of channel plasmon polaritons," Opt. Express **14**, 9467–9476 (2006).
70. S. I. Bozhevolnyi and J. Jung, "Scaling for gap plasmon based waveguides," Opt. Express **16**, 2676–2684 (2008).
71. G. B. Hocker and W. K. Burns, Mode dispersion in diffused channel waveguides by the effective index method, Appl. Opt. **16**, 113–118 (1977).
72. N. Yu, J. Fan, Q. J. Wang, C. Pflügl, L. Diehl, T. Edamura, M. Yamanishi, H. Kan, and F. Capasso, "Small-divergence semiconductor lasers by plasmonic collimation," Nat. Photonics **2**, 564–570 (2008).
73. H. J. Lezec, A. Degiron, E. Devaux, R. A. Linke, L. Martín-Moreno, F. J. García-Vidal, and T. W. Ebbesen, "Beaming light from a subwavelength aperture," Science **297**, 820–822 (2002).
74. L. Martín-Moreno, F. J. García-Vidal, H. J. Lezec, A. Degiron, and T. W. Ebbesen, "Theory of highly directional emission from a single subwavelength aperture surrounded by surface corrugations," Phys. Rev. Lett. **90**, 167401 (2003).
75. N. Yu, R. Blanchard, J. Fan, T. Edamura, M. Yamanishi, H. Kan, and F. Capasso, "Small divergence semiconductor lasers with two-dimensional plasmonic collimators," Appl. Phys. Lett. **93**, 181101 (2008).
76. N. Yu, R. Blanchard, J. Fan, Q. J. Wang, C. Pflügl, L. Diehl, T. Edamura, M. Yamanishi, H. Kan, and F. Capasso, "Quantum cascade lasers with integrated plasmonic antenna-array collimators," Opt. Express **16**, 19447–19461 (2008).
77. N. Yu, M. A. Kats, C. Pflugl, M. Geiser, Q. J. Wang, M. A. Belkin, F. Capasso, M. Fischer, A. Wittmann, J. Faist, T.

Edamura, S. Furuta, M. Yamanishi, and H. Kan, "Multibeam multi-wavelength semiconductor lasers," Appl. Phys. Lett. **95**, 161108 (2009).
78. A. Yariv and P. Yeh, *Photonics: Optical Electronics in Modern Communications* (6th ed.) (Oxford University Press, 2007).
79. H. C. Liu and F. Capasso, *Intersubband Transitions in Quantum Wells: Physics and Device Applications I* (Academic, 2000).
80. N. Yu, Q. J. Wang, C. Pflügl, L. Diehl, F. Capasso, T. Edamura, S. Furuta, M. Yamanishi, and H. Kan, "Semiconductor lasers with integrated plasmonic polarizers," Appl. Phys. Lett. **94**, 151101 (2009).
81. F. Lopez-Tejeira, Sergio G. Rodrigo, L. Martin-Moreno, F. J. Garcia-Vidal, E. Devaux, T. W. Ebbesen, J. R. Krenn, P. Radko, S. I. Bozhevolnyi, M. U. Gonzalez, J. C. Weeber, and A. Dereux, "Efficient unidirectional nanoslit couplers for surface plasmons," Nature Phys. **3**, 324–328 (2007).
82. P. G. Huggard, J. A. Cluff, G. P. Moore, C. J. Shaw, S. R. Andrews, S. R. Keiding, E. H. Linfield, and D. A. Ritchie, "Drude conductivity of highly doped GaAs at terahertz frequencies," J. Appl. Phys. **87**, 2382–2385 (2000).
83. W. Walukiewicz, L. Lagowski, L. Jastrzebski, M. Lichtensteiger, and H. C. Gatos, "Electron mobility and free-carrier absorption in GaAs: determination of the compensation ratio," J. Appl. Phys. **50**, 899–908 (1979).
84. I. I. Smolyaninov, Y.-J. Hung, and C. C. Davis, "Imaging and focusing properties of plasmonic metamaterial devices," Phys. Rev. B **76**, 205424 (2007).
85. J. Beermann, I. P. Radko, A. Boltasseva, and S. I. Bozhevolnyi, "Localized field enhancements in fractal shaped periodic metal nanostructures," Opt. Express **15**, 15234–15241 (2007).
86. I. P. Radko, V. S. Volkov, J. Beermann, A. B. Evlyukhin, T. Søndergaard, A. Boltasseva, and S. I. Bozhevolnyi, "Plasmonic metasurfaces for waveguiding and field enhancement," Laser Photon. Rev. **3**, 575–590 (2009).
87. M. Navarro-Cía, M. Beruete, S. Agrafiotis, F. Falcone, M. Sorolla, and S. A. Maier, "Broadband spoof plasmons and subwavelength electromagnetic energy confinement on ultrathin metafilms," Opt. Express **17**, 18184–18195 (2009).
88. Q. Gan, Z. Fu, Y. J. Ding, and F. J. Bartoli, "Ultrawide-bandwidth slow-light system based on THz plasmonic graded metallic grating structures," Phys. Rev. Lett. **100**, 256803 (2008).
89. B. Wang, L. Liu, and S. He, "Propagation loss of terahertz surface plasmon polaritons on a periodically structured Ag surface," J. Appl. Phys. **104**, 103531 (2008).
90. M. C. Gaidis, H. M. Pickett, C. D. Smith, S. C. Martin, R. P. Smith, and P. H. Siegel, "A 2.5-THz receiver front end for spaceborne applications," IEEE Trans. Microwave Theory Tech. **48**, 733–739 (2000).
91. P. H. Siegel and R. J. Dengler, "The dielectric-filled parabola: A new millimeter/submillimeter wavelength receiver/transmitter front end," IEEE Trans. Antennas Propag. **39**, 40–47 (1991).
92. N. Yu, Q. J. Wang, M. A. Kats, J. A. Fan, S. P. Khanna, L. Li, A. G. Davies, E. H. Linfield, and F. Capasso, "Designer spoof-surface-plasmon structures collimate terahertz laser beams," Nature Mater. doc. ID:10.1038/nmat2822 (posted 8 August 2010, in press).
93. J. Durnin, J. J. Miceli, Jr., and J. H. Eberly, "Diffraction-free beams," Phys. Rev. Lett. **58**, 1499–1501 (1987).
94. Z. Bomzon, V. Kleiner, and E. Hasman, "Formation of radially and azimuthally polarized light using space-variant subwavelength metal stripe gratings," Appl. Phys. Lett. **79**, 1587–1589 (2001).
95. R. Beth, "Mechanical detection and measurement of the angular momentum of light," Phys. Rev. **50**, 115–125 (1936).
96. M. Padgett, J. Courtial, and L. Allen, "Light's orbital angular momentum," Phys. Today 57(5) 35–40 (2004).
97. E. Cubukcu, N. Yu, E. J. Smythe, L. Diehl, K. B. Crozier, and F. Capasso, "Plasmonic laser antennas and related devices," IEEE J. Sel. Top. Quantum Electron. **14**, 1448–1461 (2008).
98. N. Yu, E. Cubukcu, L. Diehl, D. Bour, S. Corzine, J. Zhu, G. Höfler, K. B. Crozier, and F. Capasso, "Bowtie plasmonic quantum cascade laser antenna," Opt. Express **15**, 13272–13281 (2007).
99. J. N. Farahani, H.-J. Eisler, D. W. Pohl, M. Pavius, P. Flückiger, P. Gasser, and B. Hecht, "Bow-tie optical antenna probes for single-emitter scanning near-field optical microscopy," Nanotechnology **18**, 125506–125600 (2007).
100. S. Palomba and L. Novotny, "Near-field imaging with a localized nonlinear light source," Nano Lett. **9**, 3801–3804 (2009).
101. Y. A. Akimov, W. S. Koh, and K. Ostrikov, "Enhancement of optical absorption in thin-film solar cells through the excitation of higher-order nanoparticle plasmon modes," Opt. Express **17**, 10195–10205 (2009).
102. R. A. Pala, J. White, E. Barnard, J. Liu, and M. L. Brongersma, "Design of plasmonic thin-film solar cells with broadband absorption enhancements," Adv. Mater. (Weinheim, Ger.) **21**, 3504–3509 (2009).
103. E. J. Smythe, M. D. Dickey, J. Bao, G. M. Whitesides, and F. Capasso, "Optical antenna arrays on a fiber facet for in situ surface-enhanced Raman scattering detection," Nano Lett. **9**, 1132–1138 (2009).
104. Q. Xu, R. M. Rioux, M. D. Dickey, and G. M Whitesies, "Nanoskiving: A new method to produce arrays of nanostructures," Nano Lett. **41**, 1566–1577 (2008).
105. Y. Xia and G. M. Whitesides, "Soft lithography," Angew. Chem., Int. Ed. **37**, 550–575 (1998).
106. D. J. Lipomi, M. A. Kats, P. Kim, S. H. Kang, J. Aizenberg, F. Capasso, and G. M. Whitesides, "Fabrication and replication of arrays of single- or multicomponent nanostructures by replica molding and mechanical sectioning," ACS Nano **4**, 4017–4026 (2010).
107. E. J. Smythe, M. D. Dickey, G. M. Whitesides, and F. Capasso, "A technique to transfer metallic nanoscale patterns to small and non-planar surfaces," ACS Nano **3**, 59–65 (2009).